Chemical Geology 613 (2022) 121161

Contents lists available at ScienceDirect

Chemical Geology

journal homepage: www.elsevier.com/locate/chemgeo

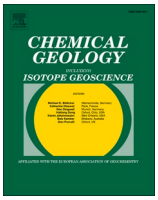

Mechanisms of Ni—Co enrichment in paleo-karstic bauxite deposits: An example from the Maochang deposit, Guizhou Province, SW China

Yufei Wang [a], Zhilin Wang [a,*], Guoxiang Chi [b], Anhuai Lu [c], Deru Xu [d], Zhilong Huang [e], Shaohao Zou [d], Teng Deng [d], Erke Peng [a], Yongzhen Long [a]

[a] Key Laboratory of Metallogenic Prediction of Nonferrous Metals and Geological Environment Monitoring, Ministry of Education, School of Geosciences and Info-Physics, Central South University, Changsha 410083, China
[b] Department of Geology, University of Regina, Regina S4S 0A2, Canada
[c] School of Earth and Space Sciences, Peking University, Beijing 100871, China
[d] State Key Laboratory of Nuclear Resources and Environment, East China University of Technology, Nanchang 330013, China
[e] State Key Laboratory of Ore Deposit Geochemistry, Institute of Geochemistry, Chinese Academy of Sciences, Guiyang 550081, China

ARTICLE INFO

Editor: Hailiang Dong

Keywords:
Pyrite
Millerite
Ni-Co enrichment
Bauxite
Maochang deposit
Guizhou Province

ABSTRACT

Many paleo-karstic bauxite deposits contain elevated concentrations of Ni and Co. It has been known that Co and Ni are dominantly hosted in sulfides, but it remains unclear how Ni and Co were incorporated into sulfides and what kind of physiochemical conditions were involved. The Maochang bauxite deposit, as one of the large Ni- and Co-bearing paleo-karstic bauxite deposits in Guizhou Province, southwest China, was selected to tackle these questions. Detailed mineralogical and sulfur isotopic analyses using integrated EBSD, EPMA, LA-ICPMS, and LA-MC-ICPMS methods revealed three stages of sulfide mineralization: stage I with pyrite (PyI), stage II with pyrite (PyII), millerite, sphalerite, chalcopyrite and violarite, and stage III with pyrite (PyIII), chalcopyrite and galena. The fine-grained, euhedral PyI has up to 0.79 wt% Ni and up to 0.53 wt% Co. In contrast, PyII, which replaced or overgrew PyI, exhibits high but variable Ni, Co and As contents, and is further divided into three sub-types: Ni-rich PyII-a (up to 16.54 wt% Ni, 0.94 wt% Co, and 0.38 wt% As) and PyII-b (up to 3.30 wt% Ni, 1.41 wt% Co, and 0.36 wt% As), and Co-rich PyII-c (up to 0.99 wt% Ni, 7.57 wt% Co, and 1.81 wt% As). PyIII is Ni- and Co-poor. Ni increases from PyI to PyIIa and PyIIb, and then decreases to PyIIc and PyIII, whereas Co remains at similar levels for PyI, PyIIa and PyIIb, significantly increases to PyIIc, and then drops abruptly to PyIII. $\delta^{34}S_{V\text{-}CDT}$ values vary dramatically from negative values for PyI (−6.9 to −16.6‰) to positive values for PyII-b (+19.4 to +22.8‰), sphalerite (+17.2 to +19.7‰), and PyIII (+25.3 to +32.3‰). Based on these results, and considering that the protoliths of the bauxites were likely Ni- and Co-rich black shales according to previous studies, a four-step model is proposed to explain the enrichment of Ni and Co in the bauxites: 1) during weathering and bauxite formation on the surface, Ni and Co were leached from the black shale together with sulfate; the metals were dissolved in the solution and partly adsorbed by Fe-oxides/hydroxides under moderate to high f_{O2}; 2) during early diagenesis, the sulfate was partially reduced to sulfide via the bacterial sulfate reduction (BSR) process and formed PyI; much of the Ni and Co, together with sulfate, remained in the solution; 3) with increasing burial, temperature increased and f_{O2} decreased, and the remaining sulfate (with elevated $\delta^{34}S_{V\text{-}CDT}$) was reduced to sulfide via the same BSR process and formed PyII; Ni was largely consumed and incorporated into PyIIa and PyIIb, whereas Co remained in the solution until precipitation of PyIIc; 4) by the time of PyIII precipitation, both Ni and Co had been taken by PyII, leaving a Ni- and Co-poor solution and PyIII. Step 1 occurred in a relatively open system, whereas steps 2–4 likely occurred in a closed system.

1. Introduction

Nickel and cobalt, listed as critical metals in many countries, attract great interest due to their significant applications in the high-technology industries of rechargeable batteries, catalysts, and superalloys (Roberts and Gunn, 2014; Hou et al., 2020). As siderophile and chalcophile

* Corresponding author.
E-mail address: wangzhilin1025@csu.edu.cn (Z. Wang).

https://doi.org/10.1016/j.chemgeo.2022.121161
Received 2 September 2022; Received in revised form 30 September 2022; Accepted 3 October 2022
Available online 12 October 2022

Table 1
Characteristics of the Ni- and/or Co-rich bauxite deposits over the world.

Deposit	Bauxite type	Assumed bauxite protolith	Ni and Co contents (ppm)	Sulfur contents	Occurrence of Ni and Co	Reference
Grebnik, Kosovo	Karstic	Ultramafic rocks and shale of the diabase-chert formation	300–7000 (Avg. 1388) Ni and 52–425 (Avg. 133) Co in bauxite		Ni-bearing chlorite	Maksimovic and Pantó (2004)
Mandan and Deh-now, Iran	Karstic	Carbonate rocks	20–294 (Avg. 168) Ni and 1–76 (Avg. 21) Co in bauxite			Zarasvandi et al. (2012)
Bidgol, Iran	Karstic	Argillaceous limestone	33–291 (Avg. 156) Ni and 2–44 (Avg. 20) Co in bauxite			Ahmadnejad et al. (2017)
Mombi, Iran	Karstic	Marly limestone	34–265 (Avg. 136) Ni and 7–44 (Avg. 24) Co in bauxite			Zamanian et al. (2016)
Shahindezh, Iran	Lateritic	Diabase	79–188 (Avg. 120) Ni and 10–274 (Avg. 109) Co in bauxite			Abedini and Calagari (2012)
Kanigorgeh, Iran	Karstic	Dolomite and limestone	5–119 (Avg. 52) Ni and 1–654 (Avg. 227) Co in bauxite			Abedini and Calagari (2014)
Kanirash, Iran	Karstic	Limestone, shale, and basalt	7–271 (Avg. 104) Ni and 10–111 (Avg. 31) Co in bauxite			Abedini et al. (2019b)
Kani Zarrineh, Iran	Karstic	Mafic rock	98–222 (Avg. 168) Ni and 85–273 (Avg. 185) Co in bauxite			Abedini et al. (2021)
Soleiman Kandi, Iran	Karstic	Mafic rock	67–574 (Avg. 275) Ni and 4–302 (Avg. 34) Co in bauxite			Abedini et al. (2022a)
Irano-Himalayan karst belt, Iran	Karstic	Basalt	33–62 (Avg. 49) Ni and 12–23 (Avg. 18) Co in bauxite		Co in Fe-oxides/ hydroxides	Abedini et al. (2022b)
Dopolan, Iran	Karstic	Argillitic dolomite	111–407 (Avg. 276) Ni in bauxite	1–5 ppm (Avg. 2.5 ppm) in bauxite		Salamab Ellahi et al. (2016)
San Giovanni Rotondo, Italy	Karstic	Distant magmatic particles and siliciclastic material	190–240 (Avg. 215) Ni and 24–49 (Avg. 31) Co in bauxite, 150–200 (Avg. 177) Ni and 12–21 (Avg. 18) Co in bauxitic claystone			Sinisi (2018)
Apulian, Italy	Karstic	Distant magmatic source and clastic material	20–590 (Avg. 433) Ni and 1–94 (Avg. 40) Co in bauxite			Mongelli et al. (2014)
Otranto, Italy	Karstic	Distant magmatic source and clastic material	140–310 (Avg. 191) Ni and 31–142 (Avg.51) Co in bauxite			Mongelli et al. (2016)
Campania Apennines, Italy	Karstic	Windblown volcanic source material and exposed terrain	82–416 (Avg. 193) Ni and 18–119 (Avg. 36) Co in bauxite			Mondillo et al. (2011)
Nurra, Italy	Karstic	Mafic rocks	60–277 (Avg. 142) Ni and 5–75 (Avg. 35) Co in bauxite, 61–187 (Avg. 124) Ni and 6–26 (Avg. 16) Co in claystone			Mameli et al. (2007)
Zagrad, Montenegro	Karstic	Shale and some UCC contents and andesitic rocks	51–298 (Avg. 121) Ni and 18–209 (Avg. 48) Co in bauxite	<0.02–0.03 wt%		Radusinović et al. (2017)
Parnassos-Ghiona, Greece	Karstic	Carbonate rocks	490–690 (Avg. 567) Ni and 10–55 (Avg. 37) Co in bauxite	3.3–4.1 wt% in red bauxite, 7.6–10.6 wt% in grey bauxite	Ni-bearing pyrrhotite, Co-bearing pentlandite	Laskou and Economou-Eliopoulos (2007)
Maochang, China	Karstic	Black shale and dolomite	4–269 (Avg. 85) Ni and 2–82 (Avg. 33) Co in aluminous rock series, 19–269 (Avg. 172) Ni and 6–135 (Avg. 59) Co in ferruginous rock series	0.01–13 wt% in bauxite, 8–34 wt% in sulfide-rich layer	Sulfide and Fe-oxides	This study Wen et al. (2021) Wu et al. (2021)
Yunfeng, China	Karstic	Dolomite and black shale	31–756 (Avg. 250) Ni and 4–69 (Avg. 39) Co in aluminous rock series, 13–909 (Avg. 261) Ni and 17–962 (Avg. 233) Co in ferruginous rock series	0.02–40 wt%	Co-rich sulfide and sulfoarsenides	Long et al. (2020)
Xiaoshanba, China	Karstic	Dolomite	23–110 (Avg. 54) Ni and 4–58 (Avg. 16) Co in aluminous rock series, 78–593 (Avg. 336) Ni and 58–63 (Avg. 60) Co in ferruginous rock series			Ling et al. (2018)
Lindai, China	Karstic	Dolomite	56–210 (Avg. 131) Ni in bauxite, 19–180 (Avg. 882) Ni in claystone, 170–297 (Avg. 234) Ni in laterite			Ling et al. (2017)
Wuchuan-Zhengan-Daozhan, China	Lateritic	Basic igneous and basic-ultrabasic intrusions	2–161 (Avg. 39) Ni in bauxite			Gu et al., 2013
Youjiang basin, China	Karstic	Volcaniclastic material	56–100 (Avg. 78) Ni in bauxite, 3–83 (Avg. 54) Ni in claystone			Yu et al., 2016
Sanhe, China	Karstic	Bauxite precursor and laterite	19–82 (Avg. 54) Ni and 2–10 (Avg. 5) Co in bauxite			Liu et al. (2017)

(*continued on next page*)

Table 1 (*continued*)

Deposit	Bauxite type	Assumed bauxite protolith	Ni and Co contents (ppm)	Sulfur contents	Occurrence of Ni and Co	Reference
Guangou, China	Karstic	Distant igneous rocks, Paleozoic carbonates, and Precambrian rocks	10–358 (Avg. 139) Ni in bauxite	95–3744 ppm (Avg. 937 ppm)		Liu et al. (2013)
Dajia, China	Karstic	Emeishan plume and carbonates	17–139 (Avg. 55) Ni in bauxite	≤0.09 wt%		Liu et al., 2010
Fusui, China	Karstic	Bauxite precursor and laterite	1–323 (Avg. 119) Ni in bauxite, 106–111 (Avg. 109) Ni in claystone, 24–56 (Avg. 40) Ni in laterite	0.01–5.65 wt%		Yu et al. (2014)
Pingguo, China	Karstic	Emeishan basalt	19–588 (Avg. 210) Ni and 2–123 (Avg. 41) Co in aluminous rock series			Wang (2019)
Dongluo, China	Karstic	Emeishan basalt	2–595 (Avg. 154) Ni and 1–202 (Avg. 30) Co in aluminous rock series			Wang, 2019
Guanmiao-Daping, China	Karstic	Dolomite	3–51 (Avg. 15) Ni and 1–33 (Avg. 7) Co in bauxite			Wang et al., 2019
Shenjiagou, China	Karstic	Dolomite	14–32 (Avg. 23) Ni and 2–6 (Avg. 4) Co in bauxite 26–63 (Avg. 49) Ni and 2–13 (Avg. 9) Co in claystone			Xu (2018)

elements, Ni and Co are preferentially incorporated into the mantle and the core of the Earth, however, diverse geological processes including magmatic, hydrothermal, and lateritic can result in the concentration of Ni and Co into the production grades. The deposit types of economic importance include lateritic Ni(—Co) (Al-Khirbash, 2015; Farrokhpay et al., 2019), sediment-hosted stratiform Cu—Co (El-Desouky et al., 2009; Qiu et al., 2021), magmatic Ni-Cu(-Co-PGE) sulfide deposits (Barnes and Lightfoot, 2005; Hughes et al., 2016) and hydrothermal vein deposits represented by the volcanogenic massive Cu—Co deposits, Ag-Co-Ni-Bi-As (five-element) vein type, unconformity-related U-Ni-Co-Cu-As deposits, and black-shale-hosted Ni(—Co) polymetallic deposits (Jefferson et al., 2007; Ahmed et al., 2009; Slack, 2012; Loukola-Ruskeeniemi and Lahtinen, 2013; Markl et al., 2016; Scharrer et al., 2019).

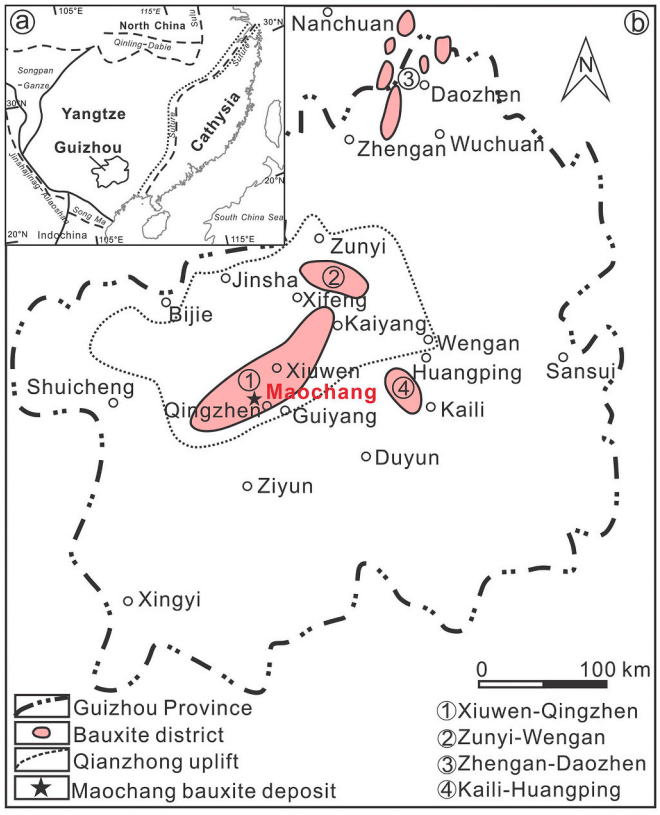

Fig. 1. (a) Inset map showing the location of the research area; (b) Sketch map illustrating the distribution of bauxite areas in Guizhou Province, South China (modified from Long et al., 2017).

Paleo-karstic bauxites, as depositional products upon the paleo-karstic topography, have the reputation not only for being an important contributor of aluminum production but also for hosting a variety of associated metals, such as Ni, Co, Li, Ga, V, Cr, rare earth elements (REE), Sc, Nb, Zr and U (e.g., Mongelli et al., 2017; Radusinović et al., 2017; Ling et al., 2020). The Ni—Co enrichment to hundreds-thousands ppm in the paleo-karstic bauxites has been reported in many deposits world widely (Table 1 and references therein), as represented by the Grebnik deposit in Kosovo (Maksimovic and Pantó, 2004), the Bidgol, Shahindezh, Kani Zarrineh, Badamlu, and Soleiman Kandi deposits in Iran (Ahmadnejad et al., 2017; Abedini et al., 2019a, 2020, 2021, 2022a), the Apulian deposit in southern Italy (Mongelli et al., 2014), and the Wachangping and Yunfeng deposits in South China (Huang et al., 2014; Long et al., 2020). It has been concluded that Ni- and Co-enriched provenances such as ultramafic-mafic rocks or black shales contributed to these metals (Table 1 and references therein), and the authigenic minerals, such as Ni-bearing chlorite (up to 6.5 wt% NiO), bravoite, cobaltiferous pyrite, pyrrhotite, pentlandite and cobaltite, were regarded as the reservoir of Ni and Co (Maksimovic and Pantó, 2004; Laskou and Economou-Eliopoulos, 2007; Long et al., 2020; Wang et al., 2021).

Sulfides, which are common in hydrothermal systems, could be produced in sedimentary and diagenetic environments in relation to fluctuating redox and pH conditions. During bauxitization, gibbsite deposited under oxidizing and acid (pH = 4.5–6.5) conditions, followed by diaspore, chamosite, siderite, and sulfide formation under reducing conditions during diagenesis (Öztürk et al., 2002; Abedini et al., 2019b). In some bauxitic profiles, sulfides may occur not only as minor minerals, but also in significant amounts in some layers, comprising part of the 'lower hematite + middle bauxite and sulfur + upper coal' stratigraphic pattern (Öztürk et al., 2002; Yu et al., 2014, 2019; Yang et al., 2019; Xiong et al., 2021). Furthermore, sulfides formed by epigenetic processes were also recognized in some bauxite deposits (Salamab Ellahi et al., 2016; Liu et al., 2010, 2017). However, it remains unclear how Ni and Co were concentrated in bauxites, specifically how nickeliferous or cobaltiferous sulfides were formed.

The Maochang paleo-karstic bauxite deposit, located at the middle Yangtze Block, is the largest concealed bauxite deposit in Guizhou

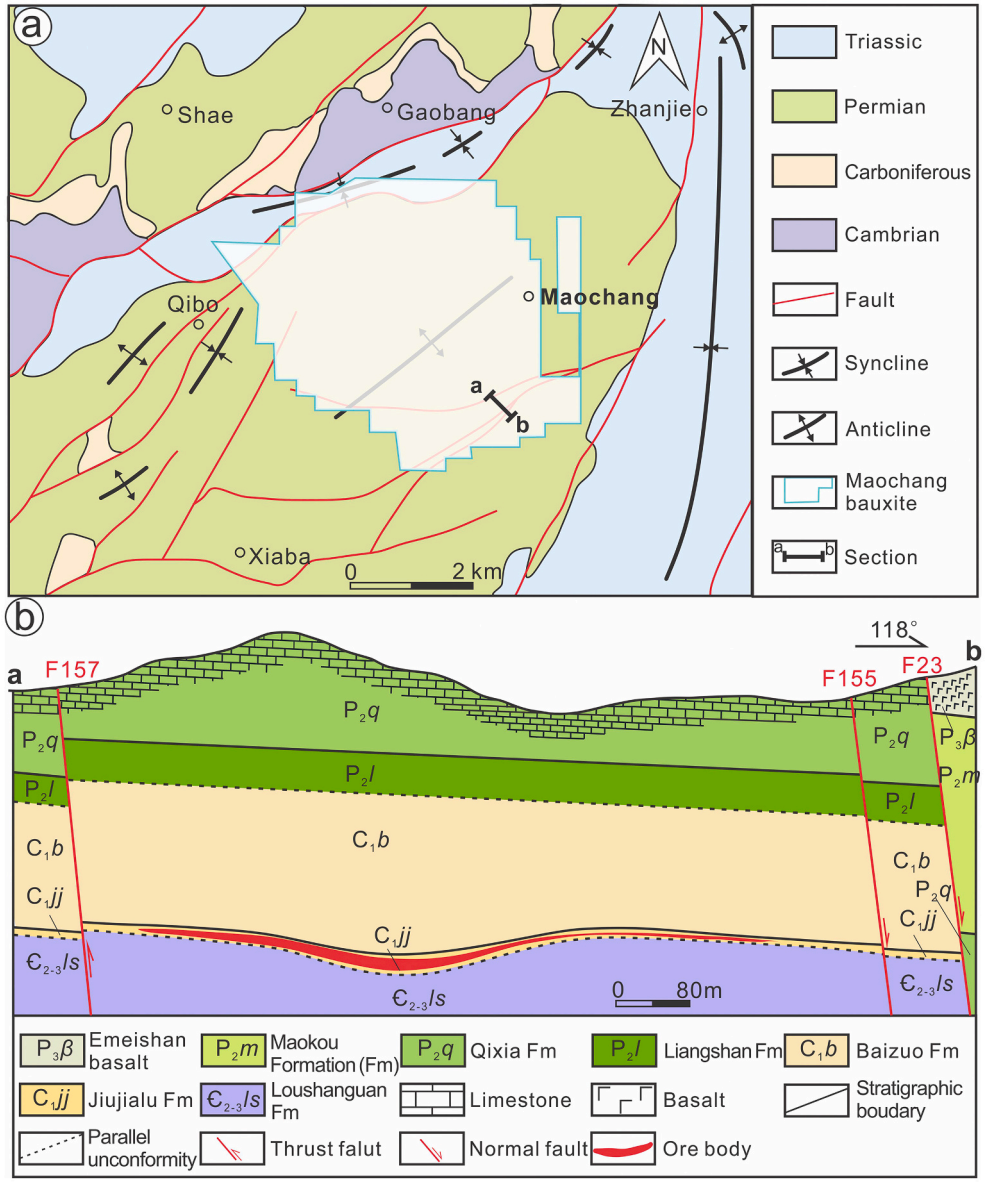

Fig. 2. (a) Simplified geological map of the Maochang bauxite deposit; (b) Simplified cross section along line a-b showing the occurrence of bauxite orebodies (modified from Wang et al., 2021).

Province, southwest China. It is characterized by high sulfur contents (up to 19.14 wt%) in bauxites and the presence of pyrite layers with thicknesses of 1.02–6.71 m in the lower and upper zones of the bauxite profiles. Recently, high Ni (up to 269 ppm) and Co (up to 135 ppm) concentrations (Wu et al., 2021) along with development of cobaltiferous pyrite (up to 9.31 wt% Co; Wang et al., 2021) have been reported in the Maochang bauxite deposit. The positive correlations of both Ni and Co contents with the sulfur contents in bauxitic rocks (Laskou and Economou-Eliopoulos, 2007; Long et al., 2020; Wu et al., 2021) indicate that these metals were possibly locked by sulfides during diagenesis to prevent them from being leached totally. If so, where were these metals originally hosted before being released and taken up by the sulfides? What kind of fluids and physiochemical conditions (e.g., Eh-pH, temperature) were involved in the remobilization and re-precipitation of the metals? Did these take place in an open or closed system?

In order to address these questions, the mineral composition and paragenesis of sulfides in the Maochang bauxite deposit were studied. Firstly, textural observations aided by backscattered electron (BSE) and electron backscatter diffraction (EBSD) were conducted. Secondly, in-situ electron probe microanalyzer (EPMA) and laser ablation-inductively coupled plasma – mass spectrometry (LA-ICP-MS) analyses were employed to reveal the complex chemical compositions of the sulfides. Then, in-situ sulfur isotope analyses by the LA-MC-ICP-MS method were used to trace the sulfur origin and evolution. These integrated studies provide detailed geochemical and mineralogical insight into the enrichment mechanisms of Ni and Co in bauxite deposits, and highlight the economic potential of high-sulfur bauxite ores considering the comprehensive utilization.

2. Geological setting

South China Block is made up of the Yangtze Block to the northwest and the Cathaysia Block to the southeast, with the amalgamation occurring during the Neoproterozoic (Yao et al., 2014; Zhao, 2015). Guizhou Province is situated within the middle and southern Yangtze Block. In this part of the Yangtze Block, Precambrian basement is overlain by fine-grained sandstone, siltstone and shale formed in Early Cambrian, followed by carbonate platform sediments of the middle to

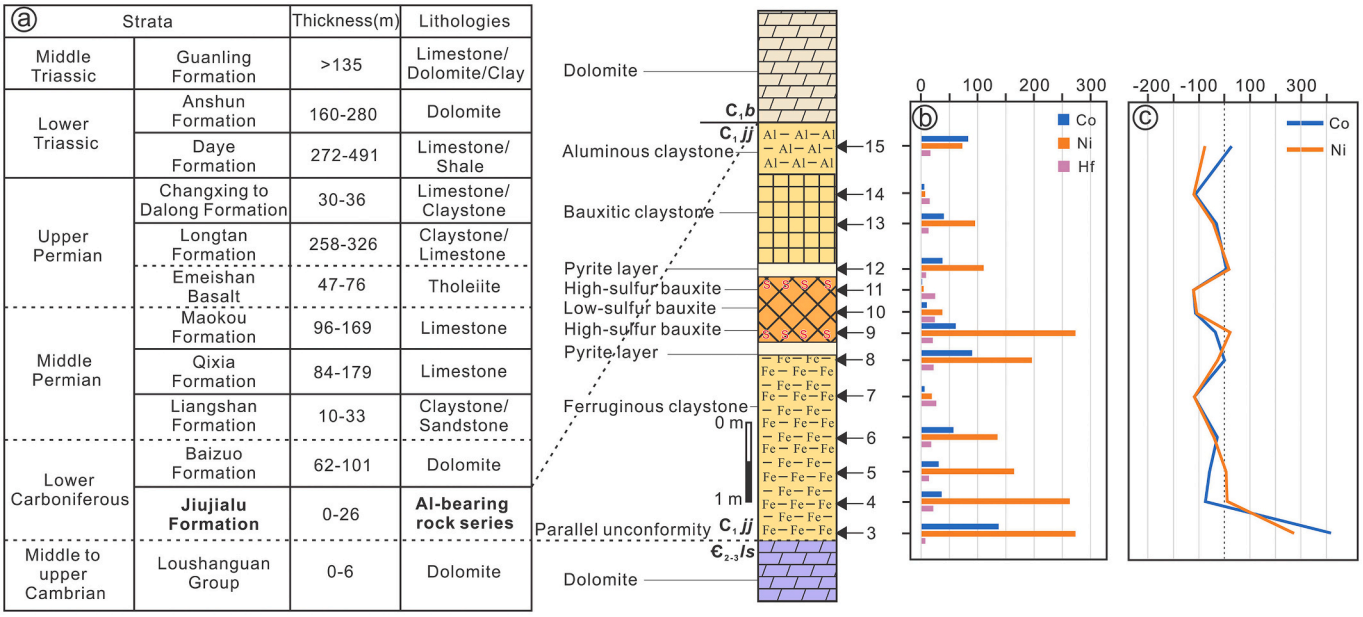

Fig. 3. (a) Stratigraphic column of the Maochang bauxite deposit and the sampling locations; (b) Profiles of Ni, Co, and Hf concentrations (ppm) across different layers; (c) Enrichment (%) of Ni and Co relative to the Upper Continental Crust (UCC) compositions by assuming Hf as an immobile element, which was calculated using the equation of $[(Co_{sample}/Hf_{sample})/(Co_{UCC}/Hf_{UCC})-1] \times 100$ and $[(Ni_{sample}/Hf_{sample})/(Ni_{UCC}/Hf_{UCC})-1] \times 100$ (Khosravi et al., 2017). The bulk concentrations of Co and Ni are from Wu et al. (2021).

upper Cambrian Loushanguan Group formed in a shallow marine environment (Chen et al., 2012). In Late Ordovician, the Duyun Movement uplifted the central Guizhou Province and formed the prototype of the Qianzhong uplift (Gao et al., 1992; Rong et al., 2011; Ling et al., 2015). The long-term denudation and peneplanation led to the development of karstic depressions and basins, i.e., a paleo-karst topography (Gao et al., 1992). Separated by a parallel unconformity (i.e., disconformity) with the underlying Loushanguan Group, the Early Carboniferous Al-bearing rock series, which was derived from the weathering of the underlying rocks (Ling et al., 2015; Long et al., 2020; Wu et al., 2021), were accumulated in the karstic depressions to form the Jiujialu Formation. The Jiujialu Formation is conformably overlain by the Early Carboniferous Baizuo Formation (GBGMR, 1987).

As one of the bauxite districts in Guizhou Province, the Xiuwen – Qingzhen bauxite area situated within the middle Qianzhong uplift (Fig. 1) hosts abundant bauxite deposits, including the Maochang, Xiaoshanba, Laowashan, Lindai, and Yunfeng deposits. Among them, the Maochang deposit is the largest concealed one, with over 200 Mt. bauxite, 6.9 Mt. pyrite and 12.74 Mt. hematite ores (Wu et al., 2021). The deposit is controlled by the broad NE-trending Daweiling anticline. The bauxite beds are crosscut by the sporadically developed NE-, NNE- and NWW-trending faults. The sedimentary rocks in the Maochang deposit generally dip less than 20°. The Paleozoic strata dominate the area, including the middle – upper Cambrian Loushanguan Group, the lower Carboniferous Jiujialu, and Baizuo formations, the middle Permian Liangshan, Qixia and Maokou formations, and the upper Permian Emeishan Basalt and Longtan and Changxing – Dalong formations (Figs. 2 and 3). In addition, the lower Triassic Daye and Anshun formations and the middle Triassic Guanling Formation are exposed in the northwestern mining area (Fig. 2a).

The Jiujialu Formation in the Maochang area, with a maximum thickness of 26 m, is composed of a set of Al-bearing rocks (Figs. 2b and 3), which can be further subdivided into two parts, i.e., a lower ferruginous rock series and an upper aluminous rock series (Figs. 4a-c). The lower ferruginous rock series is predominantly composed of red-colored ferruginous claystone and greyish-green chlorite claystone, intercalated with hematite nodule beds (Fig. 4d). Pyrite nodules and laminae are also developed in this series. The upper aluminous rock series includes the bauxite ore, bauxitic claystone, and aluminous claystone layers, from bottom to top (Figs. 4b-c). The grey bauxite layer consists of the bauxite ores with various structures including oolitic (Fig. 4e), earthy, clastic (Fig. 4f), and massive (Fig. 4g). The Al_2O_3 contents of this layer range from 49 to 76 wt%, with Al/Si ratios of 3–33 (Wu et al., 2021). Based on the sulfur contents, bauxite ores are divided into the high-sulfur (S>0.8 wt%) and low-sulfur (S ≤ 0.3 wt%) types, of which the high-sulfur bauxite ores account for about 25% of the total bauxite reserve (Zeng, 2019). In addition, pyrite layers with sulfur contents of 8.05–34.34 wt% are present in the lower and upper segments of bauxites, and are composed of kaolinite, pyrite, diaspore and chlorite. Compared with the bauxite ore layer, the bauxite-clay layer has lower Al_2O_3 (44–53 wt%) but higher SiO_2 (28–40 wt%) contents. The top light-colored aluminous claystone layer (Fig. 4c), conformably overlying the bauxite-clay layer, is composed of illite, kaolinite, chlorite and smectite, as well as minor diaspore.

Sulfides with a variety of occurrences including massive, disseminated, veins/veinlets, and stockworks are found in the Al-bearing rocks (Figs. 4h-l). Based on the field and microscopic observations, crosscutting relationships, and mineral paragenesis, three stages of sulfide mineralization have been identified in the Maochang deposit (Fig. 5). Stage I is characterized by pyrite layers and pyrite nodules or concretions (Figs. 4h-j) or disseminated, fine-grained pyrite aggregates (PyI) within a variety of Al-bearing rock series (Figs. 6a-c). In contrast, stage II is featured by diverse sulfide minerals including pyrite (reddish PyII-a and PyII-b and dark pinkish PyII-c), millerite, sphalerite, chalcopyrite, and a small amount of violarite (Figs. 6d-e and 7a-d), with siderite as the main gangue mineral. These sulfides occur as veins, veinlets, or dendrites. Stage III is featured by veins or hair-like stockworks, comprising pyrite (PyIII), chalcopyrite, and galena (Figs. 4k-l), with calcite as the major gangue mineral. Notably, all sulfide veins or veinlets exhibit sharp boundaries with the Al-bearing rock series, and no obvious alteration was observed.

2.1. Sampling and analytical methods

A total of thirteen samples from the underground tunnels, including six ferruginous claystones, four bauxite ores, two bauxitic claystones,

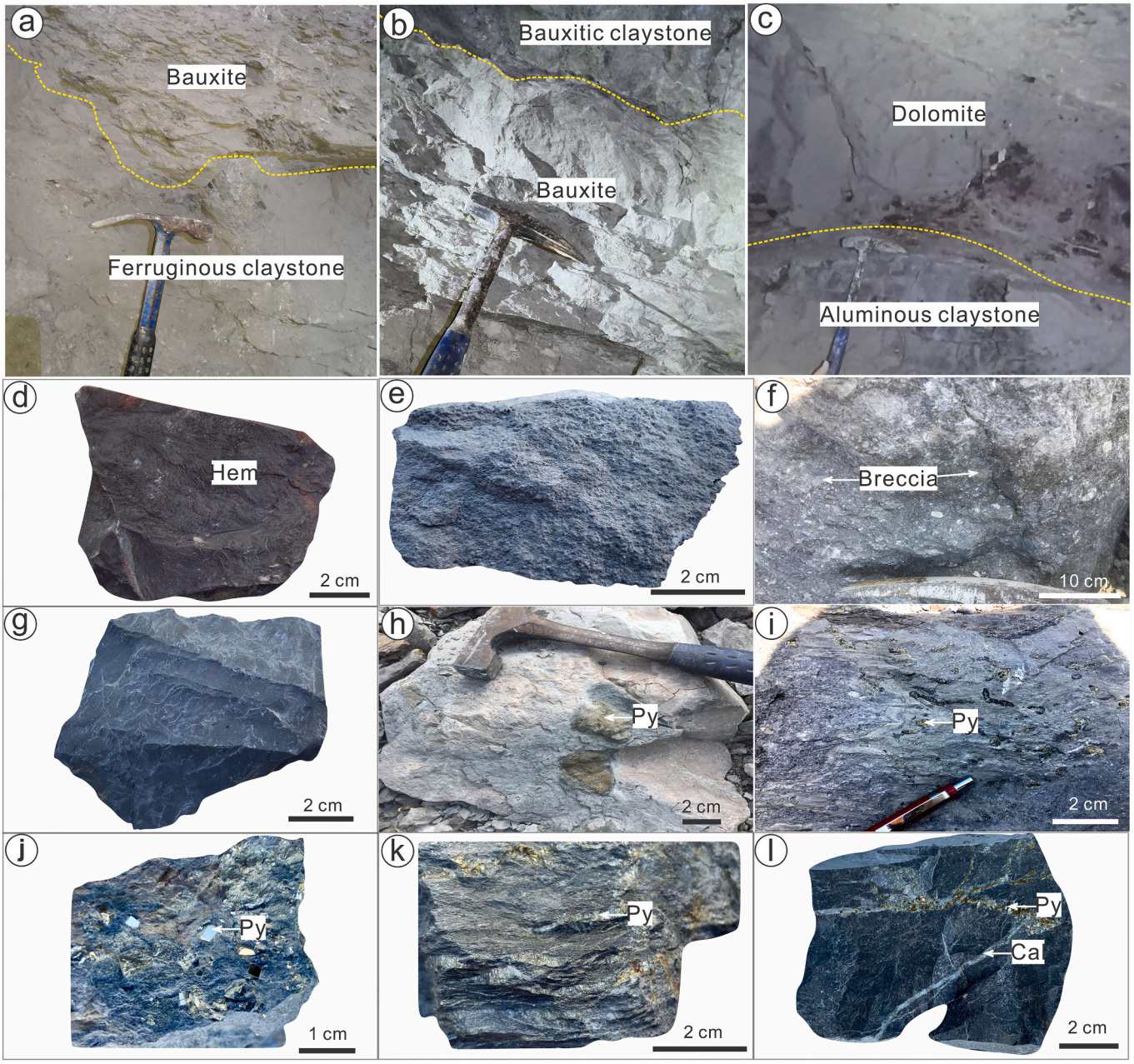

Fig. 4. Representative features of Al-bearing rock series from the Maochang bauxite deposit. (a) Conformable contact between ferruginous claystone and bauxite ore; (b) Bauxitic claystone overlying the bauxite ore; (c) Dolomite from the Baizuo Formation conformably overlying the aluminous claystone; (d) Hematite ore from the ferruginous rock series; (e) Oolitic bauxite ore; (f) Bauxite ore with a clastic texture; (g) Massive bauxite ore; (h) Massive pyrite nodules within the ferruginous claystone; (i) Scattered pyrite nodules within the bauxitic claystone; (j) Disseminated euhedral pyrite in ferruginous claystone; (k) Pyrite veins intercalated in clastic bauxite; (l) Pyrite + calcite veins in dolomite. Abbreviations: Cal = calcite, Gn = galena, Hem = hematite, Py = pyrite. Note the mineral abbreviations adapted from Whitney and Evans (2010).

and one aluminous claystone, were analyzed. The sampling locations are illustrated in Fig. 3. All in-situ analyses were carried out on polished thin sections.

Electron probe microanalysis (EPMA) was conducted using a SHIMADZU EPMA-1720 instrument equipped with four wavelength-dispersive spectrometers at the School of Geosciences and Info-Physics, Central South University. After the detailed backscattered electron (BSE) observation, spot analyses were carried out on pyrite, millerite, violarite, and hematite. Operating conditions include an accelerating voltage of 20 kV, an electron beam current of 10 nA, a beam diameter of 1 μm, and acquisition time of 30 s. Successively, three pyrite grains with complex zoning were selected for elemental mapping of Co (Kα), Ni (Kα), and As (Lβ) using wavelength dispersion spectroscopy (WDS). Operating conditions for mapping include the 20 kV acceleration voltage, 50 nA beam current, 30–80 ms sampling time for each point, 1–2 μm beam size, and 1.1 μm pitch. The EPMA data of sulfides and oxides are summarized in Tables S2 and S4–5. Detection limits were <0.01 wt% for each analyzed element. The mapping areas vary with pyrite grain sizes, with a maximum of 532 × 530 pixels.

To measure the crystallographic orientation of nickeliferous and cobaltiferous sulfides, three zones were investigated using electron backscatter diffraction (EBSD) on an FEI Quanta 450 field emission gun scanning electron microscope equipped with an Oxford Instruments HKL Nordlys II EBSD detector. In-situ EBSD analyses were carried out at State

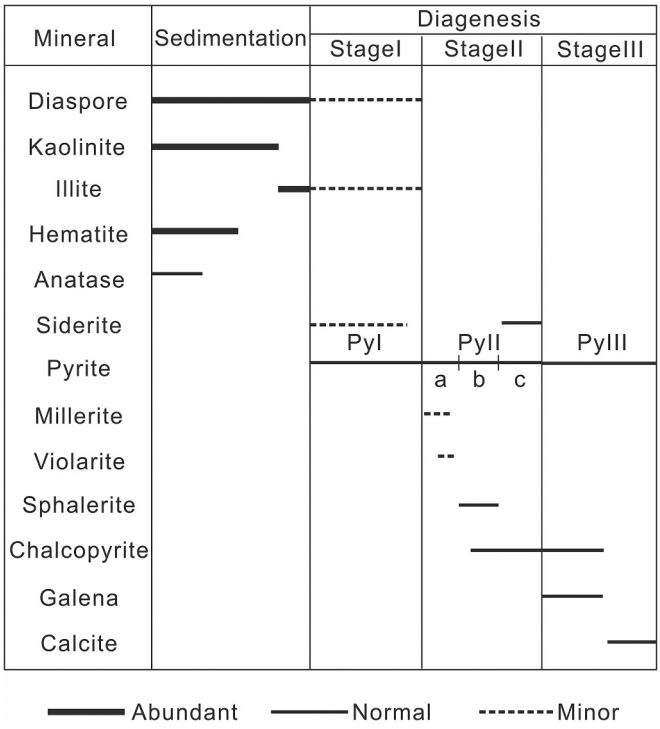

Fig. 5. Mineral paragenetic sequence in the Maochang bauxite deposit.

Key Laboratory of Geological Processes and Mineral Resources (GPMR), China University of Geosciences, Wuhan. The working voltage of 20 kV and a working distance of 25 mm were employed during the operation, and samples were tilted 70° in a low vacuum mode (20–60 Pa) to avoid excessive electron charging. The crystallographic data were collected automatically under the probe current of 5 nA, with the step sizes of 0.25–1 μm and map resolution of 246 × 347 and 240 × 170. Phase maps and inverse pole figures were generated by Tango™ software in Channel 5.

After the spot analyses by EPMA, trace element compositions of different generations of pyrite were carried out using a Telydyne Cetac HE 193 nm laser ablation system coupled with Analytik Jena Plasma-Quant MS Ellite ICP-MS at the School of Geosciences and Info-Physics, Central South University. Helium was used as a carrier gas and argon as a makeup gas. The system was operated at a constant 5-Hz pulse rate with laser energy of 2.5 J/cm^2. Pre-defined areas of thin sections were ablated using a spot size of 35 μm in diameter. Data collection consists of approximately 20 s background measurement with the laser off and 30 s data acquisition with the laser on. Elements of ^{33}S, ^{7}Fe, ^{59}Co, ^{60}Ni, ^{65}Cu, ^{75}As, ^{77}Se, ^{97}Mo, ^{107}Ag, ^{115}In, ^{118}Sn, ^{121}Sb, ^{125}Te, ^{208}Pb and ^{209}Bi were monitored during pyrite spot analyses. USGS sulfide standards MASS-1, GSE-2G, NIST SRM610, and NIST SRM612 were used for calibration as the external standards, and Fe concentrations determined by EPMA as the internal standards to calibrate trace elements in pyrite. The data reduction was performed using the GLITTER V4.4 software (Griffin et al., 2008). Minimum detection limits for pyrite were 0.29 ppm for Co, 4.55 ppm for Ni, 0.53 ppm for Cu, 1.30 ppm for As, 4.38 ppm for Se, 0.06 ppm for Mo, 0.02 ppm for Ag, 0.01 ppm for In, 0.17 ppm for Sn, 0.02 ppm for Sb, 0.11 ppm for Te, 0.05 ppm for Pb, 0.25 ppm for Bi.

In-situ sulfur isotopic analyses of pyrite and sphalerite were carried out using a combined Teledyne Cetac Technologies Analyte Excite laser-ablation system (Bozeman, Montana, USA) and Nu Instruments Nu Plasma II MC-ICP-MS (Wrexham, Wales, UK) at Nanjing FocuMS Technology Co. Ltd. The operating conditions of spot analyses include the pulse rate of 5 Hz, laser energy of 100 mJ, and beam sizes of 33 μm for pyrite and 40 μm for sphalerite, respectively. Sulfur isotopic compositions were calculated relative to the Vienna Canyon Diablo Troilite (V-CDT) standard. Natural pyrite Wenshan with the $\delta^{34}S_{V\text{-}CDT}$ value of +1.1‰ was used as the external standard. Pressed powder pellets of pyrite GBW 07267 ($\delta^{34}S_{V\text{-}CDT}$ = +3.6‰) and chalcopyrite GBW 07268 ($\delta^{34}S_{V\text{-}CDT}$ = −0.3‰) from National Research Center for Geoanalysis, China and fine-grained sphalerite SRM 123 ($\delta^{34}S_{V\text{-}CDT}$ = +17.5‰) from National Institute of Standards and Technology, U.S were treated as quality control. The result reproducibility was better than 0.6‰ (one standard deviation).

3. Results

3.1. Pyrite generations

The Ni- and Co-bearing sulfides in the Maochang deposit include pyrite and millerite, with minor violarite. Pyrite as a pervasive mineral at all stages displays complex morphological and textural characteristics. PyI commonly occurs as disseminated, fine-grained euhedral grains with sizes ranging from 10 to 150 μm in the matrix of diaspore and illite (Figs. 6a-c). Locally, PyI grains display a composite feature consisting of an inclusion (diaspore and/or illite)-rich core and a blocky rim (Fig. 6c), with homogeneous compositions.

In contrast, PyII occurs as veins cutting vertically through the bedding (Figs. 6d and 7a) and displays distinctive reflective colors relative to PyI (Figs. 6g, j and 7c). According to the crosscutting relationships and mineral assemblages, PyII could be further divided into three sub-types, i.e., PyII-a, PyII-b and PyII-c. Microscopic observations further reveal that these veins with a width smaller than 2 mm (Fig. 6d) are comprised of PyII-a in the center and PyII-b on both sides (Fig. 6e). The PyII-a veins consist of PyII-a, millerite, and minor violarite (Figs. 6f-l), of which PyII-a grains with diameters of <30 μm are characterized by the reddish reflection color and internal porosity (Fig. 6g). Noticeably, irregular blocky PyI remnants were observed in PyII-a veins (Figs. 6g-j). In contrast, anhedral PyII-b with diameters ranging from 5 to 30 μm grew predominantly with sphalerite (Figs. 6m-n). They are characterized by the dendritic growth perpendicular to PyII-a veins (Figs. 6e-f), as is typical of extensional veins. Locally, the intergrowing PyII-b and sphalerite cut across PyII-a veinlets (Figs. 6e-f), suggesting their formation slightly later than PyII-a. Comparatively, PyII-c shows a dark pinkish reflection color (Figs. 7b-c) and has close relationships with siderite (Figs. 7e-g). It replaced blocky PyI along grain boundaries and micro-fractures, with a sharp contact between them (Figs. 7b-f). In BSE images, PyII-c appears to be brighter and has higher porosity relative to PyI (Fig. 7f). No obvious correlation was observed between PyII-c and PyII-a/PyII-b.

Fine-grained PyIII together with various amounts of chalcopyrite and galena occur in hair-like veins or stockworks, with the width ranging from 5 to 200 μm (Figs. 4k-l and 7h). These veins truncated all earlier sulfide veins.

3.2. Chemical compositions

3.2.1. Pyrite

A total of 75, 34, 12, 13, and 29 spot analyses with EPMA were carried out on PyI, PyII-a, PyII-b, PyII-c, and PyIII, respectively (Table S1). All spots yielded low Se, Sb, and Pb concentrations varying from below the detection limits (b.d.l) to 0.15, 0.24, and 0.38 wt%, respectively, and highly variable Ni, Co, and As contents (Figs. 8-9). The PyI has Ni, Co, and As contents from b.d.l to 0.79 wt% (Avg. 0.29 wt%), 0.02 to 0.53 wt% (Avg. 0.09 wt%), and 0.15 to 0.45 wt% (Avg. 0.24 wt%), respectively. In comparison, PyII shows a wide variation of Co, Ni, and As. PyII-a has the highest Ni concentrations (1.01–16.54 wt%; Avg. 3.48 wt%), and low Co (0.02–0.94 wt%; Avg. 0.15 wt%) and As concentrations (b.d.l – 0.38 wt%; Avg. 0.23 wt%). Compared to PyII-a, PyII-b has lower Ni (1.06–3.30 wt%; Avg. 2.09 wt%) but higher Co (0.12–1.41 wt%; Avg. 0.64 wt%) concentrations. The highest Co (1.18–7.57 wt%; Avg. 6.02 wt%) and As (0.04–1.81 wt%; Avg. 1.36 wt

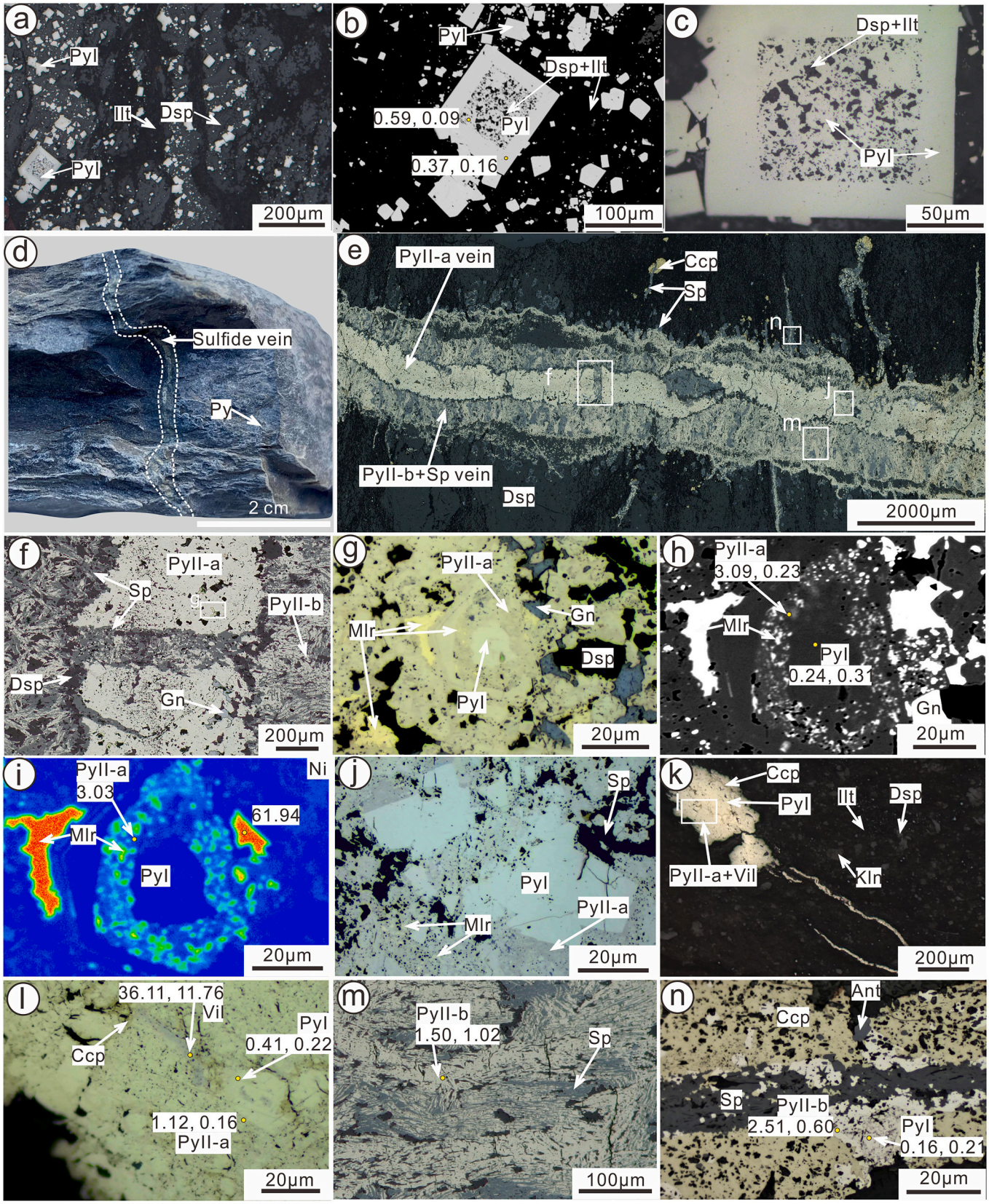

(caption on next page)

Fig. 6. The occurrence of PyI and nickeliferous pyrite (PyII-a, PyII-b) and their texture and paragenesis in the Maochang bauxite deposit. (a) Euhedral PyI disseminated in the ferruginous claystone, reflective light; (b) BSE image of (a); (c) PyI characterized by an inclusion-rich core and a compact rim, reflective light; (d) Sulfide vein truncating bauxite ore; (e) Sulfide vein in (d) consisting of pyrite (PyII-a) in the middle and intergrowing pyrite (PyII-b) and sphalerite in the remaining parts of the vein, reflective light; note PyII-b crosscuts PyII-a; (f) Dendritic PyII-b and sphalerite cutting across the PyII-a vein, reflective light; (g) Porous, reddish Ni-rich PyII-a and millerite replacing early PyI irregularly, reflective light with Gamma image enhancement; (h) BSE image of (g); (i) Nickel elemental distribution of (h) by WDS mapping; (j) Porous Ni-rich PyII-a along with millerite replacing euhedral PyI, with PyI remnant like isolated islands, reflective light; (k-l) Pyrite veins in the ferruginous claystone; note Ni-rich PyII-a together with violarite and chalcopyrite replacing PyI, reflective light; (m) Dendritic Ni- and Co-rich PyII-b and sphalerite tangled with each other, reflective light; (n) PyI remnants within the Ni-rich PyII-b, reflective light. The quantitative values represent the Ni (left) and Co (right) concentrations (wt%), respectively. Abbreviations: Ant = anatase, Ccp = chalcopyrite, Dsp = diaspore, Gn = galena, Ilt = illite, Kln = kaolinite, Mlr = millerite, Py = pyrite, Sp = sphalerite, Vil = violarite.

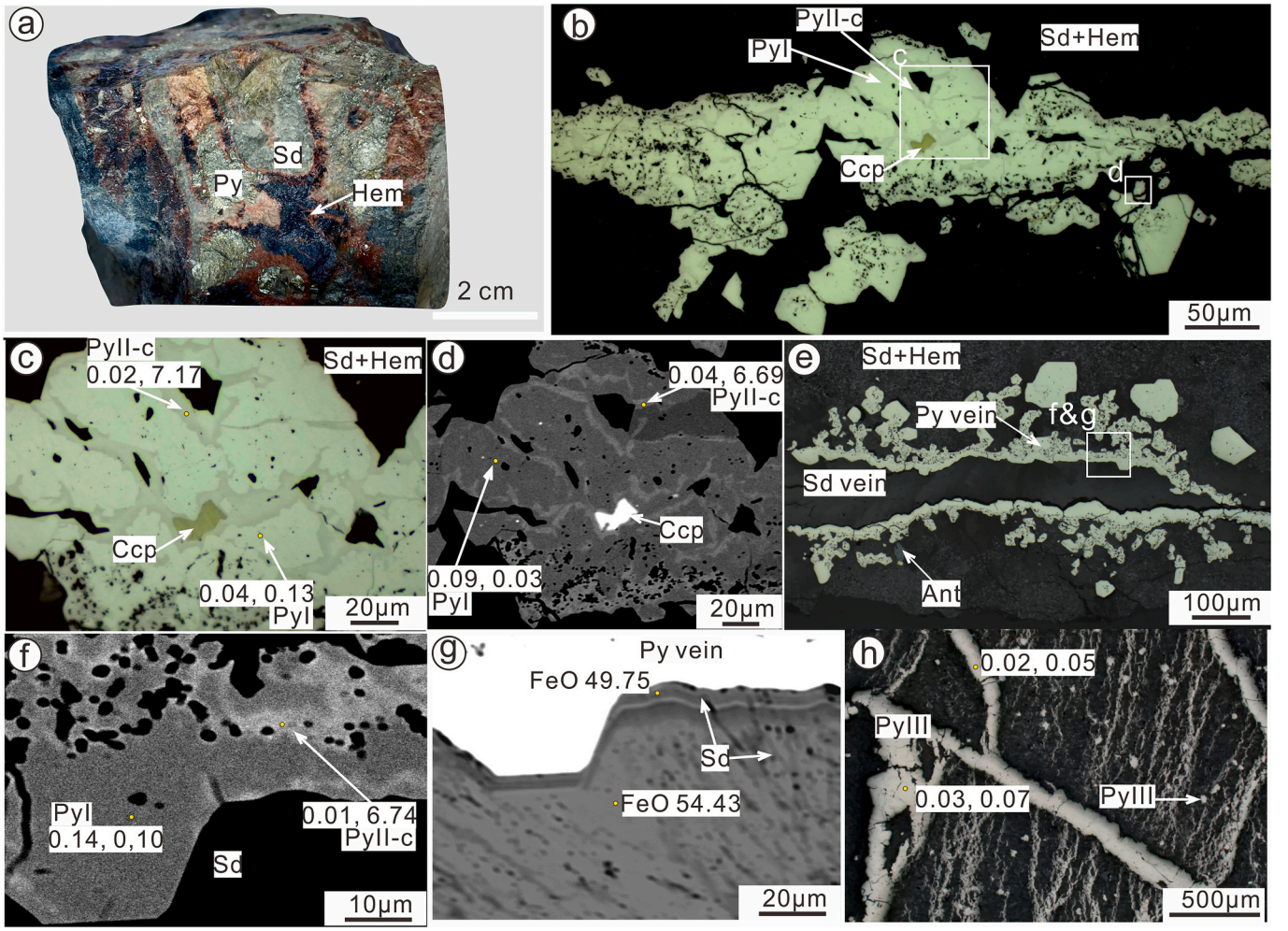

Fig. 7. The occurrences of PyI, PyII-c, and PyIII and their textures and paragenesis in the Maochang bauxite deposit. (a) Sulfides and siderite in ferruginous claystone; (b-c) Sulfide veins in (a) consisting of PyI, dark pinkish Co-rich PyII-c and chalcopyrite; note PyII-c replacing PyI, reflective light with Gamma image enhancement; (d) BSE image of (c); (e-g) A siderite vein truncating a pyrite vein; note Co-rich PyII-c replaces PyI as shown in (f) (BSE) and the dark siderite in contact with the pyrite vein has lower FeO content as shown in (g) (BSE); (h) Hair-like and thick PyIII veins in ferruginous claystone, reflective light. The quantitative values represent the Ni (left) and Co (right) concentrations (wt%), respectively. Abbreviations: Ant = anatase, Ccp = chalcopyrite, Dsp = diaspore, Hem = hematite, Ilt = illite, Py = pyrite, Sd = siderite.

%) concentrations were found in PyII-c, accompanied by a sharply decreasing Ni concentration (b.d.l – 0.99 wt%; Avg. 0.12 wt%). These results reveal a negative correlation of Fe with Ni in PyII-a and PyII-b (Fig. 9b) and with Co in PyII-c (Fig. 9c), indicating both Ni and Co incorporation into pyrite by substituting Fe, rather than as inclusions. In addition, negative correlations of As with both S (Fig. 9d) and Fe (Fig. 10a) were observed in cobaltiferous PyII-c. In combination with a strong positive correlation between As and Co (Fig. 9e), the plot of PyII-c along the (Co, Fe)$(As_xS_{1-x})_2$ trend line in the diagram of 2As/S vs 2(Fe + Co + Ni)/S (Fig. 10b) favors As (As^-) substituting S, rather than As (As^{2+} or As^{3+}) substituting Fe (Deditius et al., 2008). As for PyIII, it has the low Co (0.02–0.13 wt%; Avg. 0.06 wt%), Ni (b.d.l – 0.08 wt%; Avg. 0.04 wt %) and As (0.16–0.74 wt%; Avg. 0.29 wt%) contents.

Given that most PyII grains with complex patchy or zoning textures have diameters of <20 μm, LA-ICP-MS analyses of PyII were not considered. A total of 24 spots were analyzed including 14 for PyI and 10 for PyIII (Table S2). All analyses show low Ga, Ge, and Mo concentrations varying from b.d.l to several ppm. The Co, Ni, Cu, As, Se, Te, Ag, In, and Sn contents are highly variable between PyI and PyIII. Generally, PyI displays relatively high Co (0.86–397 ppm), Ni (19.72–3102 ppm), Se (13.9–40.91 ppm), Ag (0.4–5.96 ppm), In (0.03–9.86 ppm) and Sn (0.27–4.41 ppm) contents, whereas PyIII is enriched in Cu (22.55–9662

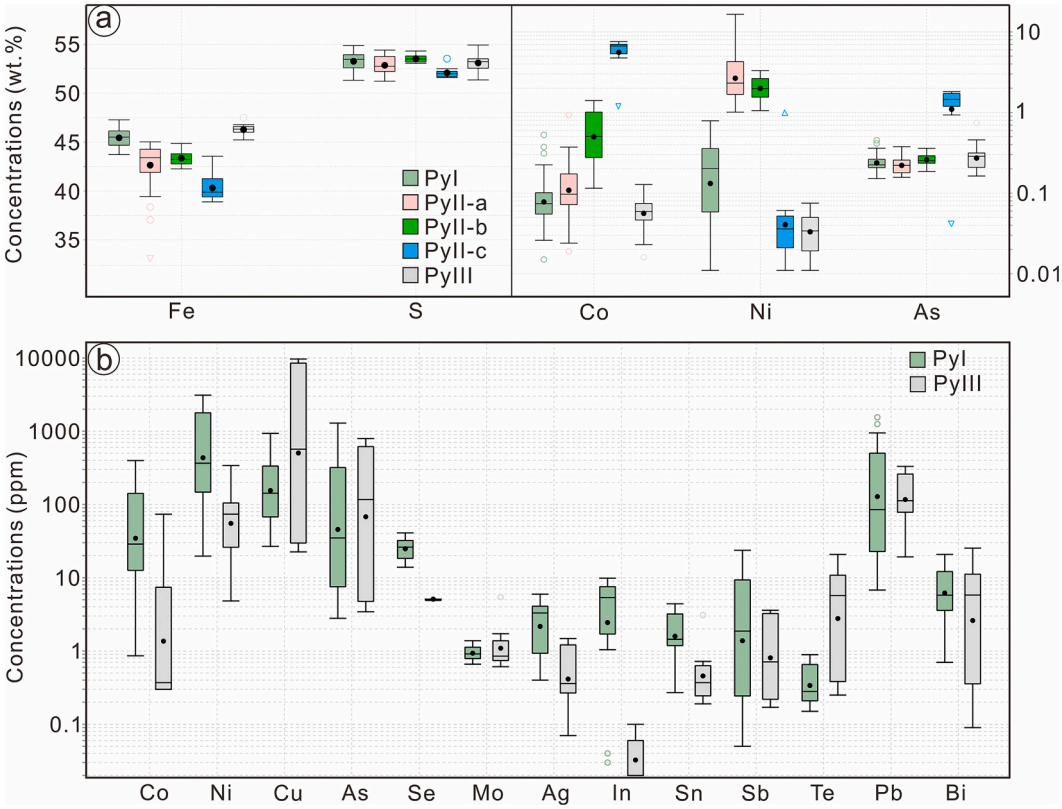

Fig. 8. Box and whisker plots showing the chemical compositions of pyrite analyzed by EPMA (a) and LA-ICPMS (b).

ppm) and Te (0.25–20.82) (Fig. 8b). Arsenic contents in PyI (2.79–1289 ppm; Avg. 236 ppm) are similar to that of PyIII (3.43–794 ppm; Avg. 285 ppm).

3.2.2. Millerite and violarite

Due to the small sizes, only 6 millerite and 2 violarite spots were analyzed with EPMA (Table S3). Millerite has Ni contents from 61.21 to 62.14 wt%, S contents from 34.81 to 36.80 wt% and Fe contents from 2.52 to 3.48 wt%. The contents of Co and As in millerite are no >0.1 wt %. In contrast, violarite has higher S (41.41–41.86 wt%), Co (11.76–12.14 wt%) and Fe (7.24–8.92 wt%) contents, and lower Ni contents (36.11–37.64 wt%), showing a deviation from the Ni end-member in the Co-Fe-Ni ternary diagram (Fig. 11).

3.2.3. Hematite

Six EPMA spot analyses were obtained for the chemical compositions of hematite (Table S4). Hematite has Fe contents of 90.61–91.46 wt%, with minor MgO (0.05–0.09 wt%, Avg. 0.07 wt%), CoO (0.09–0.16 wt%, Avg. 0.13 wt%) and Cr_2O_3 (0.06–0.09 wt%, Avg. 0.08 wt%).

3.3. WDS mapping of pyrite

WDS X-ray mapping was undertaken for selected pyrites from different stages with complex textures (Figs. 12 and 13). The mapping results reveal that the zoning patterns of pyrite under the microscope were mainly caused by the inhomogeneous occurrence of Ni, Co, and As. In a composite pyrite with PyI and PyII-a, the PyII-a is characterized by Ni-rich zones intergrowing with millerite and has a sharp contact with the PyI remnant (Fig. 12). Interestingly, Ni and Co in PyII-a exhibit a decoupling behavior (Fig. 12a). In a composite pyrite with PyI, PyII-c and PyIII, the PyII-c is characterized by Co-rich zones and also has a sharp boundary with PyI, whereas PyIII is low in Ni, Co, and As (Fig. 13). Similarly, the mapping displays the dichotomy of Ni and Co in PyII-c. Both Co and As show similar zoning patterns in PyII-c, with the highest concentrations near the contact with PyI (Fig. 13).

3.4. EBSD analyses of Ni- and Co-bearing sulfides

The EBSD mappings display the complex textural features of Ni- and Co-bearing sulfides. The phase mapping affirms the inconsistency of the crystal systems between pyrite and millerite (Figs. 14b, e and h). The *Z*-inverse pole fig. (Z-IPF) mapping reveals that single PyI grains in reflected light photomicrographs (Figs. 14a and d) are actually composed of several pyrite grains with different orientations (Figs. 14c and f), as shown by the clear grain boundaries. Meanwhile, the Z-IPF mapping also confirms that PyII-a and PyII-c share the same crystallographic orientation with PyI (Figs. 14c, f and i), whereas the temporally and spatially associated PyII-a and millerite have different crystallographic characteristics (Figs. 14c and f), most likely due to their distinct crystal systems.

3.5. Sulfur isotope compositions

A total of 31 in-situ sulfur isotopic analyses were completed, of which 4 spots are from PyI, 6 spots from PyII-b, 14 spots from PyIII, and 7 spots from sphalerite (Table S5). The PyII-a and PyII-c grains were excluded from LA-MC-ICPMS sulfur isotopic analyses due to their small sizes. The PyI has negative $\delta^{34}S_{V\text{-}CDT}$ values varying from −16.6 to −6.9‰ (Avg. -13.6‰), whereas PyII-b yields positive $\delta^{34}S_{V\text{-}CDT}$ values ranging from +19.4 to +22.8‰ (Avg. +21.1‰). In comparison, PyIII has the most elevated $\delta^{34}S_{V\text{-}CDT}$ values of +25.3 to +32.3‰ (Avg. +28.8‰). Overall, the $\delta^{34}S_{V\text{-}CDT}$ values of pyrite fall into two distinct populations, i.e., negative values for PyI, and positive values for PyII and PyIII (Fig. 15).

Sphalerite coexisting with PyII-b yields the $\delta^{34}S_{V\text{-}CDT}$ values ranging from +17.2 to +19.7‰ (Avg. +18.1‰), slightly lower than that of PyII-b and PyIII (Fig. 15b). In combination with the absence of sulfate and Fe-oxide formation during these stages, $\delta^{34}S_{V\text{-}CDT}$ values of pyrite and

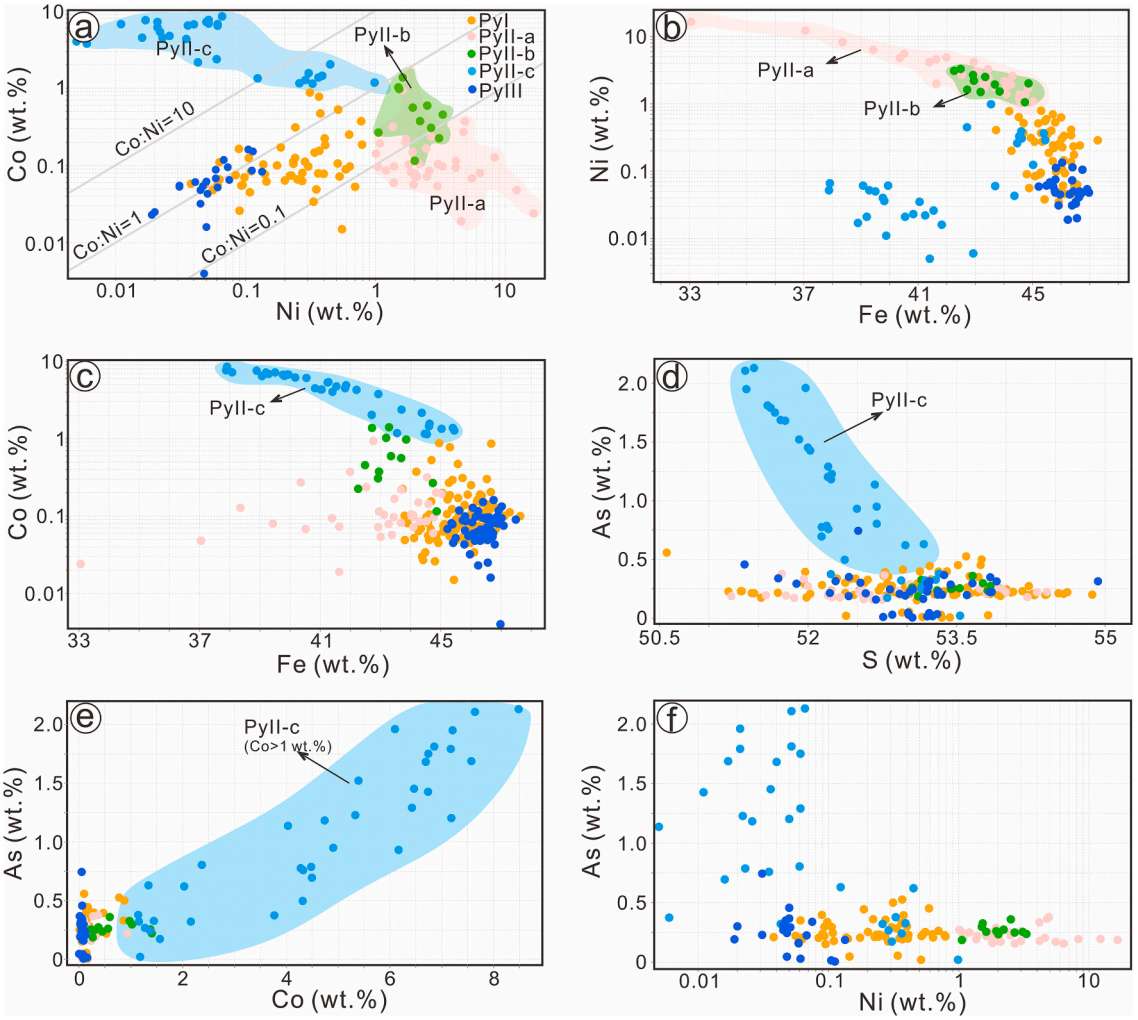

Fig. 9. Binary plots of Co—Ni (a), Ni—Fe (b), Co—Fe 9 (c), As—S (d), As—Co (e), and As—Ni (f) for pyrites from the Maochang deposit. The EPMA data shown in the diagrams include results from this study and data from Wang et al. (2021).

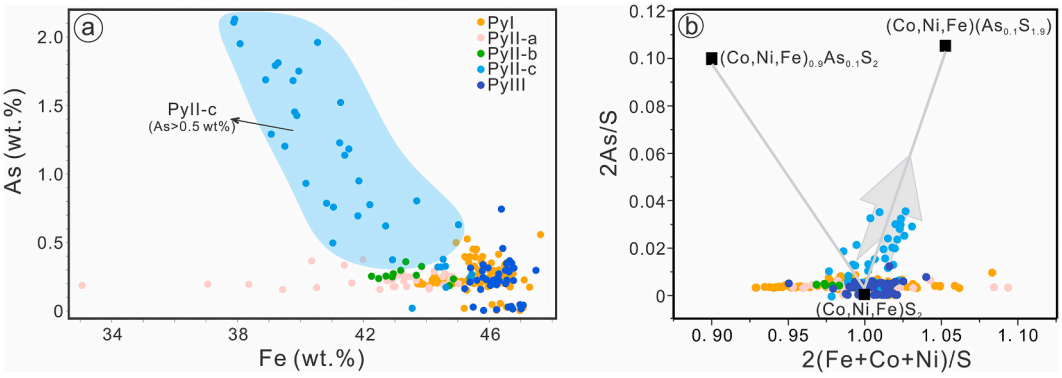

Fig. 10. Binary plots of Fe vs. As (a) and 2(Fe + Co + Ni)/S vs. 2As/S (b). The latter shows the As^{-} substitution of S, instead of cationic As substitution of Fe. The EPMA data in this study and data from Wang et al. (2021) were applied.

sphalerite could be used as the S isotope signature of the total sulfur of the fluids (Ohmoto and Goldhaber, 1997).

4. Discussion

During the formation of karstic bauxites, the aluminum-rich provenance, paleoclimate, paleogeography, regional tectonics, and exposure duration are crucial factors (Bogatyrev et al., 2009; Abedini and Calagari, 2012; Yu et al., 2016, 2019; Liu et al., 2017; Hou et al., 2017; Khosravi et al., 2021; Xiong et al., 2021; Yang et al., 2021; Abedini et al., 2022b). Previous research demonstrates that the Carboniferous paleokarstic bauxite deposits in the central Guizhou uplift were generally derived from weathering of underlying units on the western margin of the Yangtze Block (Ling et al., 2013, 2017; Wang et al., 2018; Wu et al.,

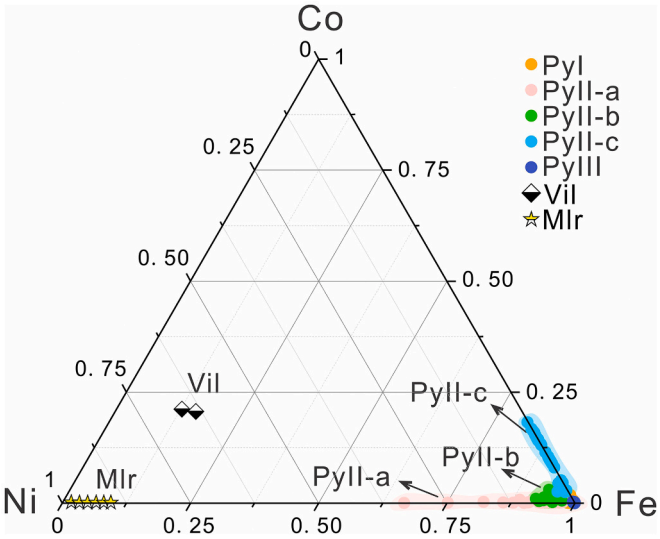

Fig. 11. Ternary diagram showing the Fe-Co-Ni compositions of pyrite, millerite, and violarite from the Maochang bauxite deposit. The EPMA data in this study and data from Wang et al. (2021) were used.

2021), with Ni and Co provided by the lower Cambrian black shales (i.e., the Niutitang Formation, Long et al., 2017, 2020). These black shales host a conformable thin polymetallic Ni-Mo-PGE-Au sulfide ore horizon (Mao et al., 2002; Jiang et al., 2007). The similar REE patterns as well as the positive correlations shown in the TiO_2 vs. Zr, TiO_2 vs. Th, Al_2O_3 vs. TiO_2, Th vs. Ta, Nb vs. Th, and Nb vs. Ta diagrams (based on data from Wu et al., 2021) between the Maochang Al-bearing rock series and the black shales also confirm their affinity.

With the proceeding denudation and peneplanation during the Qianzhong uplift, the weathering products were subsequently accumulated in the karstic depressions dominantly as simple Al- and Fe/Ti oxides (e.g., gibbsite, geothite, and hematite) along with clay minerals (e.g., kaolinite and illite) to form the prototype of bauxite (Zhuang et al., 2016). These initial bauxite mineral phases point to the acidic and oxidizing conditions of surface water (Temur and Kansun, 2006). Although Ni and Co can be transported by weathering aqueous fluids even at ambient temperature (Liu et al., 2011; Migdisov et al., 2011; Williams-Jones and Vasyukova, 2022), part of them were likely fixed by adsorption on Fe oxides and hydroxides during chemical weathering (Mao et al., 2002; Mongelli et al., 2017; Abedini et al., 2019b). Support for this Ni and Co fixation mechanism includes: 1) positive correlations of Ni and Co with Fe_2O_3 rather than Al_2O_3 among the Al-bearing rock series (Wu et al., 2021), 2) high Ni (up to 269 ppm) and Co (up to 135 ppm) concentrations in the ferruginous claystone sequence (Figs. 3b-c), and 3) high CoO concentrations (up to 0.16 wt%) in authigenic hematite from the ferruginous claystone (Table S4). This Co and Ni fixation process resembles the Ni—Co mineralization during the lateritization of mafic/ultramafic rocks (Freyssinet et al., 2005; Kamenetsky et al., 2016; Ugwu and Sherman, 2017).

When the karstic topography subsided and was subsequently capped by the overlying sequences during the transgression, the Maochang bauxite and clay horizons evolved to the diagenetic stage. Mineral dehydration as represented by the transformation of boehmite/gibbsite to diaspore occurred through this stage (Ahmadnejad et al., 2017). As the environment transformed from oxidizing to reducing due to microbial activity-related oxygen consumption (Allen, 2002; Liu et al., 2017), sulfides were formed by the reduction of interstitial dissolved sedimentary sulfates (Öztürk et al., 2002; Laskou and Economou-Eliopoulos, 2007), which could be traced by sulfur isotopes (Ohmoto and Goldhaber, 1997; Qiu et al., 2021). The Maochang PyI has $\delta^{34}S_{V\text{-}CDT}$ values of −6.9 to −16.6‰ (Fig. 15), lower than that of the Cambrian to Triassic seawater sulfate (+20 to +28‰; Kampschulte and Strauss, 2004). The large sulfur fractionation between sulfate and sulfide was most likely derived from bacterial sulfate reduction (BSR), by which $\delta^{34}S_{V\text{-}CDT}$ values of 2–46‰ lighter than the seawater sulfate could be produced (Canfield and Teske, 1996; Habicht et al., 1998). The presence of BSR is also evidenced by the ferruginous microspherules formed by microbial activities (Zhou et al., 2006), the presence of evaporite residue (e.g., barite) and the high TOC contents (0.02–4.76 wt%, av. 0.51 wt%; Yang et al., 2019) in pyrite layer. Moreover, the abundance of iron-oxides/hydroxides in the Maochang bauxite possibly provided Fe for diagenetic pyrite (Abedini et al., 2019b), as reflected by the replacement of iron-oxides/hydroxides by pyrite (Fig. 7a). The contents of up to 0.79 wt% Ni and 0.53 wt% Co in PyI revealed that minor amounts of Ni and Co were incorporated into pyrite lattice during the early diagenesis.

Distinct from the negative $\delta^{34}S_{V\text{-}CDT}$ values of PyI, PyII-b and coexisting sphalerite yielded positive $\delta^{34}S_{V\text{-}CDT}$ values of +19.4 to +22.8‰ and + 17.2 to +19.7‰, respectively (Fig. 15). Considering the diagenetic depth of <4 km (Long et al., 2017, 2020) and weak tectonic activities, the mineralizing temperature of sulfides was likely lower than

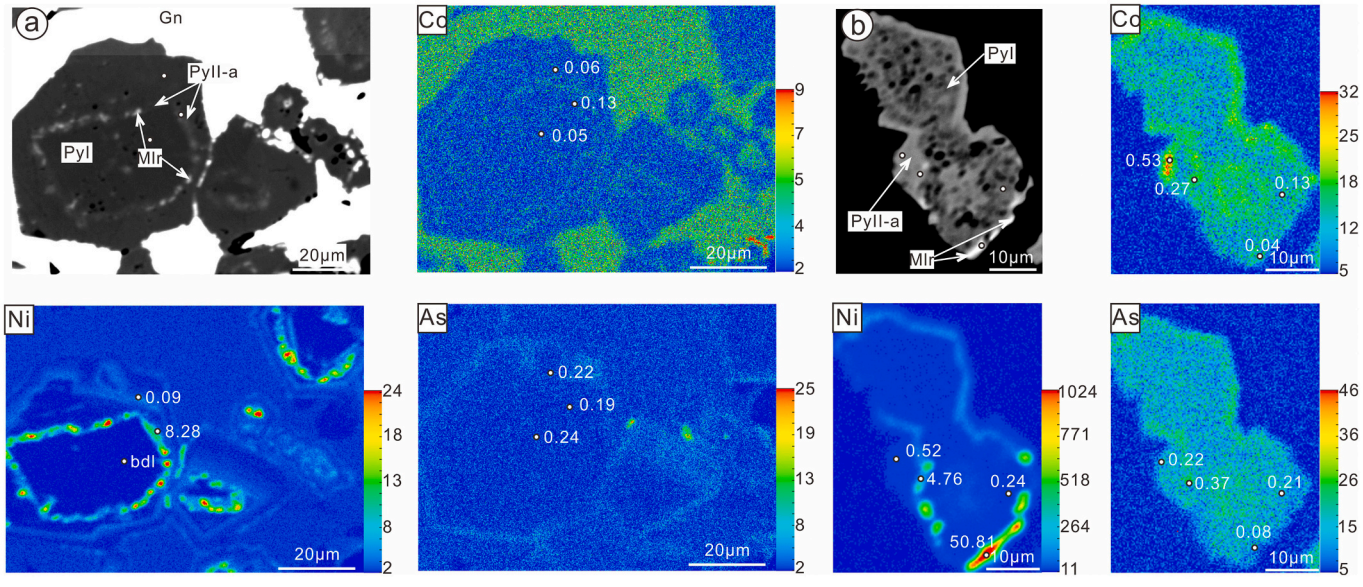

Fig. 12. (a-b) WDS mapping of Co, Ni, and As for Ni-rich pyrite grains. Marked values (wt%) of Co, Ni, and As contents are from EPMA data.

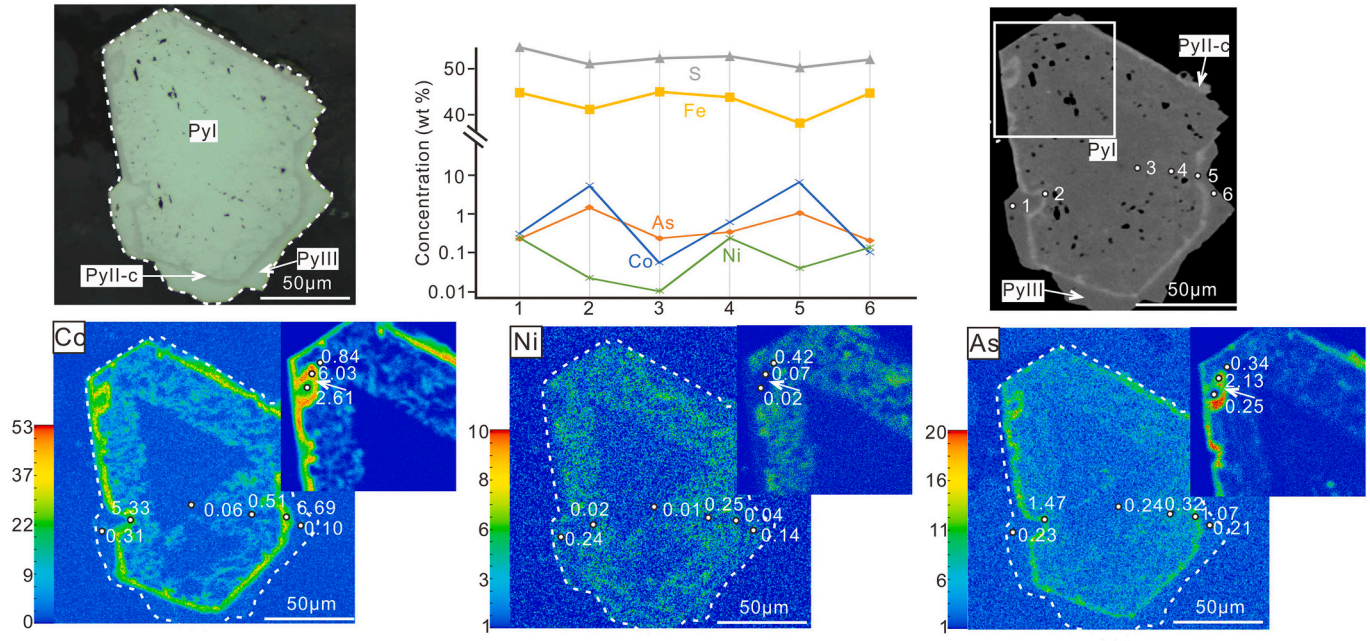

Fig. 13. WDS mapping of Co, Ni, and As for a Co-rich pyrite grain, and the variation of chemical compositions. Marked values (wt%) of Co, Ni, and As contents are from EPMA data. Note the ultra-enrichment of Co and As at the reaction front.

120 °C, and thus the mechanism of abiotic thermochemical reduction of sulfate (TSR), which requires temperatures over 160–180 °C (Machel, 2001), can be precluded. Instead, the small fractionations ($\triangle^{34}S_{sulfate\text{-}sulfide}$ <11‰) at stage II were possibly ascribed to the sequential BSR process in a closed system where sulfate supply is restricted (Eldridge et al., 1993; Habicht et al., 2002). In detail, due to PyI enriched in the light sulfur isotope during reduction, the residual sulfates in the closed system became much heavier, and the late-stage pyrites (PyII and PyIII) likewise became heavier, like its parent SO_4^{2-} (Xue et al., 2015; Goldhaber, 2003). The general evolution trend of sulfur isotopes towards heavier values through time can also be reflected in the sedimentary columns and sediment-hosted sulfide deposits in sedimentary basins (Eldridge et al., 1993; Goldhaber, 2003; Xue et al., 2015).

PyII with elevated Ni and Co concentrations commonly replaces the earlier PyI pseudomorphically (Figs. 12 and 13). The replacement is likely caused by fluid-mediated coupled dissolution and reprecipitation process (CDR) rather than solid-state diffusion (Liu and Beaudoin, 2021), due to the sharp and truncating contact between PyII and PyI, consistent morphology and crystallographic orientation as revealed by EBSD (Fig. 14). This is also supported by the fine-grained millerite with the miss-match of lattice parameters (Figs. 6d-f) as part of the zoning patterns together with nickeliferous PyII-a. Considering the close temporal and spatial association between millerite and nickeliferous PyII-a, the supersaturation at the reaction interface during the CDR process possibly nucleated millerite (Altree-Williams et al., 2015). Combined with the weak host rock alteration, these textures indicate a fast fluid-mineral interaction possibly caused by far-from-equilibrium conditions (Markl et al., 2016; Burisch et al., 2017).

A sequential precipitation of PyII-a followed by PyII-b is observed, whereas there is no direct crosscutting relationships between PyII-c and PyII-a or PyII-b. Relative to PyII-a and b, the presence of siderite with lower FeO contents at the contact front with PyII-c (Fig. 7g) indicates that PyII-c precipitated at the end of the paragenetic sequence as the progressive dissolution of CO_2 contributed by consumption of reductants (e.g. TOC) and increasing HCO_3^- activity would lead to siderite precipitation (Markl et al., 2016; Burisch et al., 2017). Remarkably, the chemical compositions of PyII display a dichotomy, i.e., Ni enriched in PyII-a (1.01–16.54 wt% Ni and 0.02–0.94 wt% Co) and PyII-b (1.06–3.30 wt% Ni and 0.12–1.41 wt% Co) and Co enriched in PyII-c (b.d.l-0.99 wt% Ni and 1.18–7.57 wt% Co) (Figs. 9a and 11). Given the absence of pyrrhotite in the Maochang deposit, the possibility that Ni was preferentially incorporated into pyrrhotite and Co into coexisting pyrite caused the decoupling of Ni and Co can be ruled out (e.g., Loukola-Ruskeeniemi, 1999; Clark et al., 2004; Cook et al., 2011; Veloso et al., 2020). Instead, the dichotomy may be affected by the contrasting physio-chemical conditions during proceeding diagenesis because the solubility of Ni and Co in fluids and the stability of their sulfide minerals are a function of temperature, pH, oxygen fugacity (f_{O2}), and reduced sulfur activity (Liu et al., 2011; Tian et al., 2012; Scharrer et al., 2019, 2021; Williams-Jones and Vasyukova, 2022; Vasyukova and Williams-Jones, 2022). In the Maochang deposit, the As contents show a sharp increase from PyII-a (<0.50 wt%) and PyII-c (up to 1.81 wt%), indicating a decreasing f_{O2} that transformed AsO_3^{3-} species in fluids into As^{1-} during Co-rich PyII-c precipitation. Moreover, the consumption of H^+ during the reduction of AsO_3^{3-} would also increase the pH values at which Ni is less soluble than Co (Markl et al., 2016). Taking these together, decreasing f_{O2} and increasing pH in fluids are considered as the main factors accounting for the dichotomy of Ni and Co, while other factors such as temperature and sulfur activity may not be important as there is no relevant evidence in the Maochang deposit. It is interesting to note that similar mineral succession from Ni- to Co- arsenides is common in five-element vein deposits worldwide (e.g., Ahmed et al., 2009; Markl et al., 2016; Burisch et al., 2017; Scharrer et al., 2019, 2021; Guilcher et al., 2021).

After Ni and Co were considerably incorporated by PyII, the solution became Ni- and Co-poor, and the subsequently precipitated PyIII has low concentrations of Ni and Co. In addition, PyIII displays slightly higher $\delta^{34}S_{V\text{-}CDT}$ values (+25.3 to +32.3‰) relative to PyII (Fig. 15), which was likely caused by the continuous BSR process in a closed diagenetic system with the limiting sulfate supply (Öztürk et al., 2002; Yang et al., 2021).

In view of the above discussions, a four-step model of Ni—Co mineralization in the Maochang deposit was constructed (Fig. 16). Firstly, the weathering of carbonates of the underlying Loushanguan Group and black shales of the Niutitang Formation contributed to deposition of bauxite-bearing rock series in which Ni and Co were either

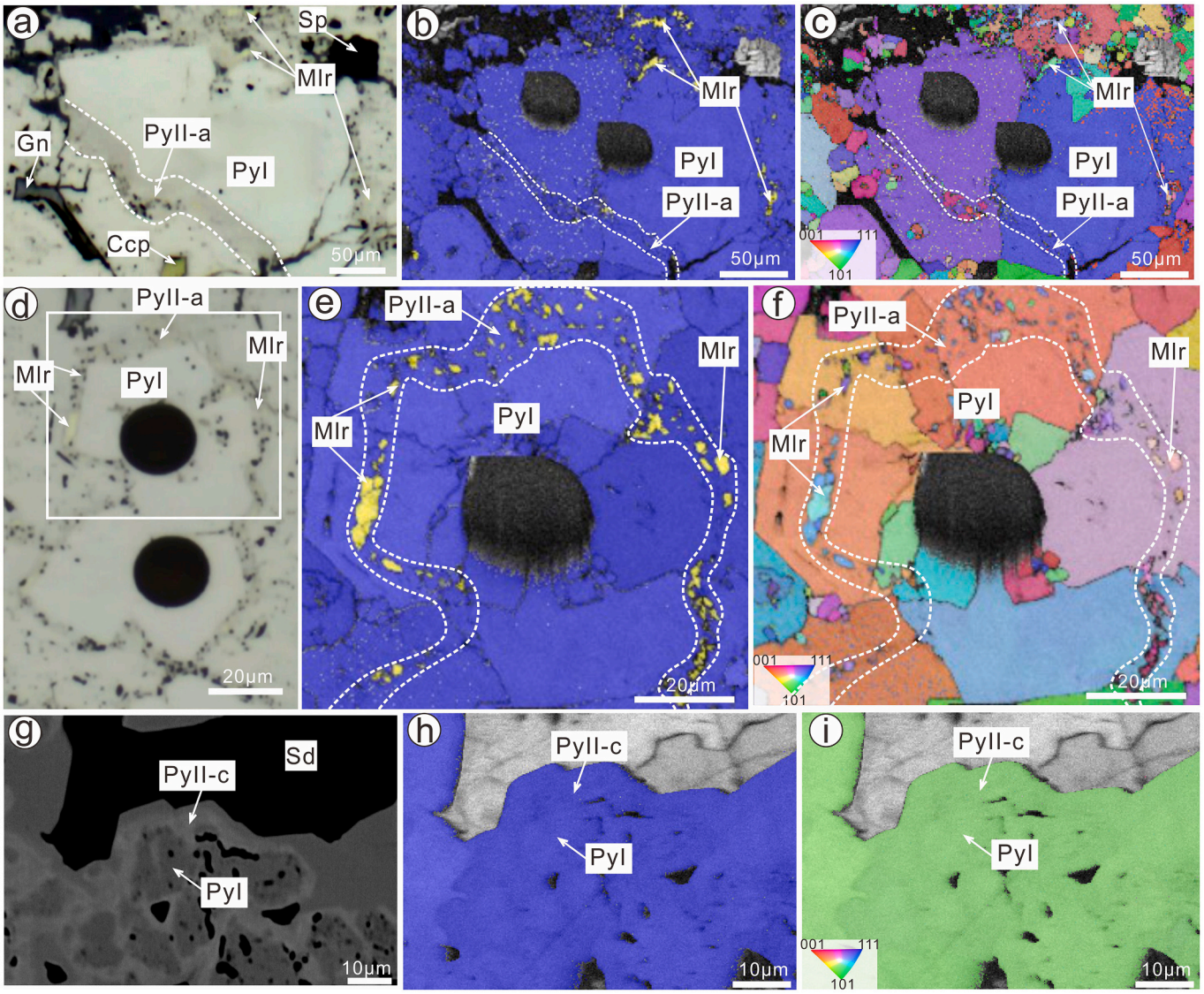

Fig. 14. (a-c) Ni-rich PyII-a along with millerite cutting across PyI grains; (d-f) Ni-rich PyII-a and millerite truncating several PyI grains; note the consistent crystallographic orientation between PyII-a and PyI and distinct crystallographic orientations between millerite and pyrite; (g-i) Co-rich PyII-c exhibiting a consistent crystallographic orientation with PyI. Note (a) and (d) are photomicrographs; (g) is BSE image; (b), (e), and (h) are EBSD phase maps; and (c), (f), and (i) are EBSD inverse pole maps. Abbreviations: Ccp = chalcopyrite, Gn = galena, Mlr = millerite, Py = pyrite, Sd = siderite, Sp = sphalerite.

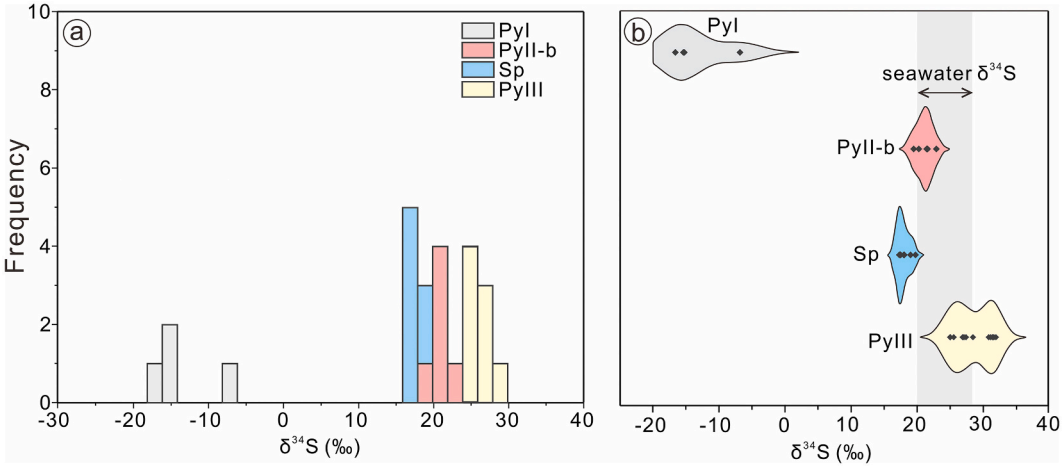

Fig. 15. Histogram (a) and violin diagram (b) of $\delta^{34}S_{V\text{-}CDT}$ values for pyrite and sphalerite from the Maochang bauxite deposit.

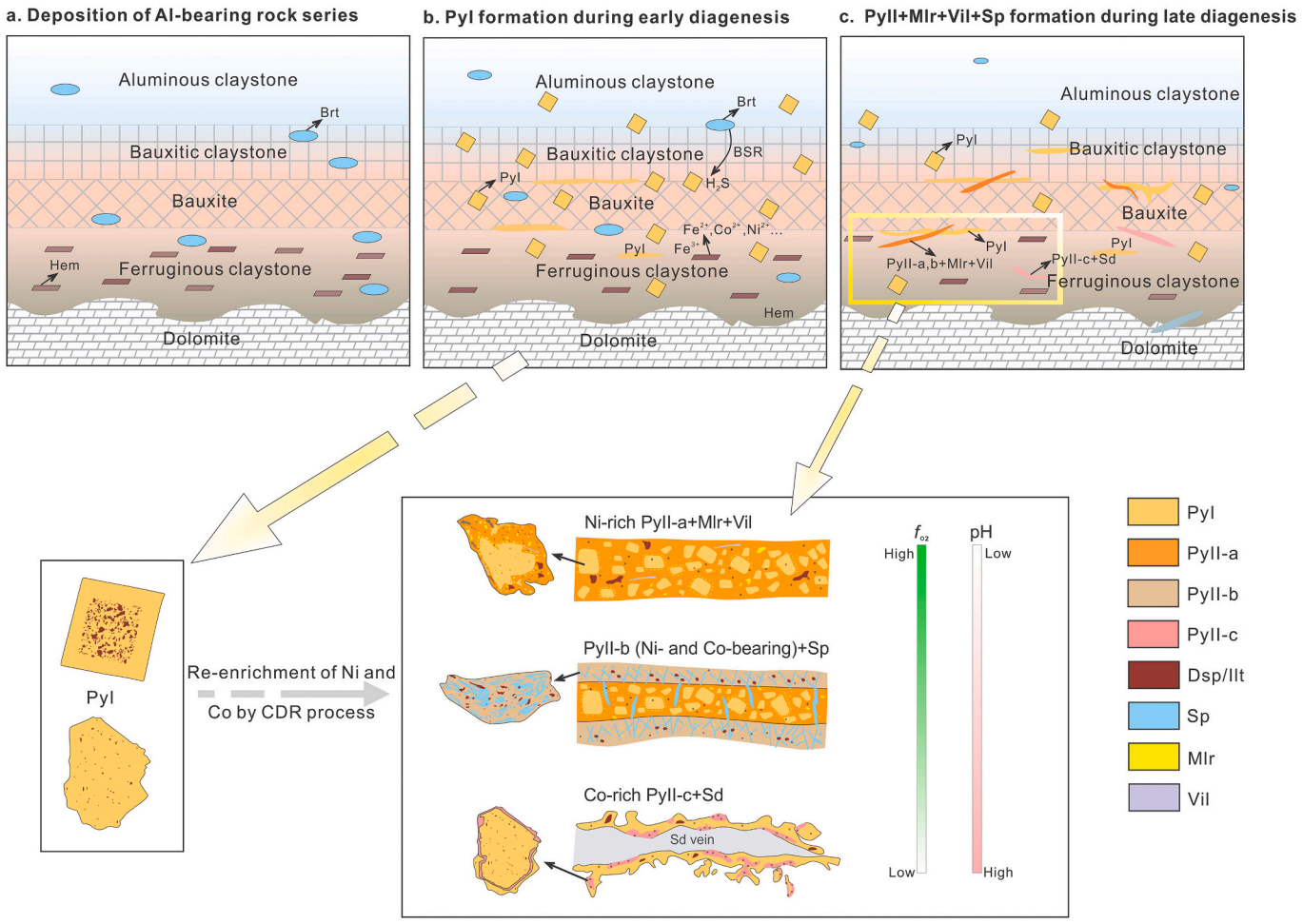

Fig. 16. Schematic model illustrating the process of Ni and Co enrichment in the Maochang bauxite deposit. (a) Deposition of the Al-bearing rock series with Ni and Co absorbed by Fe-oxides/hydroxides under moderate to high f_{O2}; (b) Ni—Co release from Fe-oxides/hydroxides and incorporation into PyI during early diagenesis, with PyI formed by reduction of the oxidized, sulfate-bearing fluids via BSR process; (c) Remobilization of Ni and Co and re-precipitation as Ni- and Co-rich PyII and millerite during burial diagenesis, in which decreasing f_{O2} and increasing pH caused Ni precipitation earlier than Co. Abbreviations: Brt = barite, Dsp = diaspore, Hem = hematite, Ilt = illite, Mlr = millerite, Py = pyrite, Sd = siderite, Sp = sphalerite, Vil = violarite.

dissolved in the solution or absorbed on Fe-oxides/hydroxides under moderate to high f_{O2} (Fig. 16a). Secondly, during early diagenesis, the oxidized, sulfate-bearing fluids were reduced through BSR and formed PyI; meanwhile, minor Ni and Co were incorporated into PyI (Fig. 16b). Thirdly, with increasing burial, the remaining sulfate was reduced via the continuous BSR process to form as PyII in a closed system, in which Ni was taken up mainly by PyII-a and PyII-b and Co by PyII-c corresponding to decreasing f_{O2} and increasing pH (Fig. 16c). Finally, the Ni- and Co-poor solution precipitated PyIII as both Ni and Co had been mostly consumed by PyII. Consequently, the Ni—Co enrichment in the bauxite deposits was the product of karstic basin evolution through multiple periods of fluid activity from an open to a closed system, in which sulfur played a key role in retaining Ni and Co during diagenesis. Thus, much attention should be paid to the economic potential of sulfides and their associated critical metal resources in the bauxite deposits, considering the abundance of karstic bauxite resources in the world.

5. Conclusion

Three stages of sulfide mineralization including PyI (up to 0.79 wt% Ni and up to 0.53 wt% Co), PyII (up to 16.54 wt% Ni and 7.57 wt% Co) + millerite + sphalerite + chalcopyrite + violarite, and PyIII (up to 0.13 wt% Co and 0.08 wt% Ni) + chalcopyrite + galena, were identified in the Maochang paleo-karstic bauxite deposits. The abundance of nickeliferous and cobaltiferous sulfides indicate that sulfur controlled the retention of Ni and Co in bauxites. The trend of S isotopes from negative $\delta^{34}S_{V\text{-}CDT}$ values for PyI (−6.9 to −16.6‰) to positive $\delta^{34}S_{V\text{-}CDT}$ values for PyII-b (+19.4 to +22.8‰), sphalerite (+17.2 to +19.7‰), and PyIII (+25.3 to +32.3‰) reveals that the sulfides formed via the continuous bacterial sulfate reduction (BSR) processes in a close diagenetic system. The dichotomy of Ni and Co in sulfides (i.e., the successive evolution from millerite and Ni-rich PyII-a and PyII-b to the Co-rich PyII-c) reflects the changing physico-chemical conditions (i.e., decreasing f_{O2} and increasing pH). The formation of Ni- and Co-rich bauxites involves an initial Ni and Co dissolution and absorption on Fe-oxides/hydroxides in a relatively open, supergene environment with moderate to high f_{O2}, followed by Ni and Co incorporation into sulfides in a closed, reducing, digenetic environment. This study highlights the importance of multistage evolution of karstic basins for the Ni—Co enrichment in the bauxite deposits, apart from the Ni- and Co-rich protolith.

Declaration of Competing Interest

The authors declare that they have no known competing financial interests or personal relationships that could have appeared to influence the work reported in this paper.

Data availability

Data will be made available on request.

Acknowledgments

This research was financially co-supported by the National Natural Science Foundation of China (No. 41672077, 41930428) and Hunan Provincial Natural Science Foundation of China (No. 2021JJ30817). We sincerely thank Penglin Cheng from Galuminium Group Co., Ltd. for his field assistance. A particular thank is given to two anonymous reviewers and Editor-in-Chief Hailiang Dong for their thorough and constructive reviews.

Appendix A. Supplementary data

Supplementary data to this article can be found online at https://doi.org/10.1016/j.chemgeo.2022.121161.

References

Abedini, A., Calagari, A.A., 2012. The mineralogy and geochemistry of Permian lateritic ores in east of Shahindezh, West-Azarbaidjan province, Iran. J. Crystallogr. Mineral. 20, 59–72.

Abedini, A., Calagari, A.A., 2014. REE geochemical characteristics of titanium-rich bauxites: the Permian Kanigorgeh horizon, NW Iran. Turk. J. Earth Sci. 23, 513–532. https://doi.org/10.3906/yer-1404-11.

Abedini, A., Rezaei Azizi, M., Calagari, A.A., 2019a. REE tetrad effect as a powerful indicator of formation conditions of karst bauxites: a case study of the Shahindezh deposit, NW Iran. Acta Geol. Sin. 93, 912–927. https://doi.org/10.1111/1755-6724.13763.

Abedini, A., Habibi Mehr, M., Khosravi, M., Calagari, A.A., 2019b. Geochemical characteristics of the karst-type bauxites: an example from the Kanirash deposit, NW Iran. Arab. J. Geosci. 12, 1–16. https://doi.org/10.1007/s12517-019-4601-z.

Abedini, A., Khosravi, M., Dill, H.G., 2020. Rare earth element geochemical characteristics of the late Permian Badamlu karst bauxite deposit, NW Iran. J. Afr. Earth Sci. 172, 103974 https://doi.org/10.1016/j.jafrearsci.2020.103974.

Abedini, A., Mongelli, G., Khosravi, M., 2021. Geochemical constraints on the middle Triassic Kani Zarrineh karst bauxite deposit, Irano-Himalayan belt, NW Iran: implications for elemental fractionation and parental affinity. Ore Geol. Rev. 133, 104099 https://doi.org/10.1016/j.oregeorev.2021.104099.

Abedini, A., Mongelli, G., Khosravi, M., 2022a. Geochemistry of the early Jurassic Soleiman Kandi karst bauxite deposit,Irano-Himalayan belt, NW Iran: constraints on bauxite genesis and thedistribution of critical raw materials. J. Geochem. Explor. 241, 107056 https://doi.org/10.1016/j.gexplo.2022.107056.

Abedini, A., Khosravi, M., Mongelli, G., 2022b. The middle Permian pyrophyllite-rich ferruginous bauxite, northwestern Iran, Irano-Himalayan belt, NW Iran: constraints on elemental fractionation and provenance. J. Geochem. Explor. 233, 106905 https://doi.org/10.1016/j.gexplo.2021.106905.

Ahmadnejad, F., Zamanian, H., Taghipour, B., Zarasvandi, A., Buccione, R., Salamab Ellahi, S., 2017. Mineralogical and geochemical evolution of the Bidgol bauxite deposit, Zagros Mountain Belt, Iran: Implications for ore genesis, rare earth elements fractionation and parental affinity. Ore Geol. Rev. 86, 755–783. https://doi.org/10.1016/j.oregeorev.2017.04.006.

Ahmed, A.H., Arai, S., Ikenne, M., 2009. Mineralogy and paragenesis of the Co-Ni arsenide ores of Bou Azzer, Anti-Atlas, Morocco. Econ. Geol. 104, 249–266. https://doi.org/10.2113/gsecongeo.104.2.249.

Al-Khirbash, S., 2015. Genesis and mineralogical classification of Ni-laterites, Oman Mountains. Ore Geol. Rev. 65, 199–212. https://doi.org/10.1016/j.oregeorev.2014.09.022.

Allen, R., 2002. Role of diffusion–precipitation reactions in authigenic pyritization. Chem. Geol. 182, 461–472. https://doi.org/10.1016/S0009-2541(01)00334-5.

Altree-Williams, A., Pring, A., Ngothai, Y., Brugger, J., 2015. Textural and compositional complexities resulting from coupled dissolution–reprecipitation reactions in geomaterials. Earth Sci. Rev. 150, 628–651. https://doi.org/10.1016/j.earscirev.2015.08.013.

Barnes, S.-J., Lightfoot, P.C., 2005. Formation of magmatic nickel-sulfide ore deposits and processses affecting their copper and platinum-group element contents. Econ. Geol. 179–213. https://doi.org/10.5382/AV100.08.

Bogatyrev, B., Zhukov, V., Tsekhovsky, Y.G., 2009. Formation conditions and regularities of the distribution of large and superlarge bauxite deposits. Lithol. Miner. Resour. 44, 135–151. https://doi.org/10.1134/S0024490209020035.

Burisch, M., Gerdes, A., Walter, B.F., Neumann, U., Fettel, M., Markl, G., 2017. Methane and the origin of five-element veins: Mineralogy, age, fluid inclusion chemistry and ore forming processes in the Odenwald, SW Germany. Ore Geol. Rev. 81, 42–61. https://doi.org/10.1016/j.oregeorev.2016.10.033.

Canfield, D.E., Teske, A., 1996. Late Proterozoic rise in atmospheric oxygen concentration inferred from phylogenetic and sulphur-isotope studies. Nature 382, 127–132. https://doi.org/10.1038/382127a0.

Chen, X., Zhang, Y.D., Fan, J.X., Tang, L., Sun, H.Q., 2012. Onset of the Kwangsian Orogeny as evidenced by biofacies and lithofacies. Sci. China Earth Sci. 55, 1592–1600. https://doi.org/10.1007/s11430-012-4490-4.

Clark, C., Grguric, B., Mumm, A.S., 2004. Genetic implications of pyrite chemistry from the Palaeoproterozoic Olary Domain and overlying Neoproterozoic Adelaidean sequences, northeastern South Australia. Ore Geol. Rev. 25, 237–257. https://doi.org/10.1016/j.oregeorev.2004.04.003.

Cook, N.J., Ciobanu, C.L., Danyushevsky, L.V., Gilbert, S., 2011. Minor and trace elements in bornite and associated Cu–(Fe)-sulfides: A LA-ICP-MS study. Geochim. Cosmochim. Acta 75, 6473–6496. https://doi.org/10.1016/j.gca.2011.08.021.

Deditius, A.P., Utsunomiya, S., Renock, D., Ewing, R.C., Ramana, C.V., Becker, U., Kesler, S.E., 2008. A proposed new type of arsenian pyrite: Composition, nanostructure and geological significance. Geochim. Cosmochim. Acta 72, 2919–2933. https://doi.org/10.1016/j.gca.2008.03.014.

El-Desouky, H.A., Muchez, P., Cailteux, J., 2009. Two Cu–Co sulfide phases and contrasting fluid systems in the Katanga Copperbelt, Democratic Republic of Congo. Ore Geol. Rev. 36, 315–332. https://doi.org/10.1016/j.oregeorev.2009.07.003.

Eldridge, C., Williams, N., Walshe, J.L., 1993. Sulfur isotope variability in sediment-hosted massive sulfide deposits as determined using the ion microprobe SHRIMP: II. a study of the HYC deposit at McArthur River, Northern Territory, Australia. Econ. Geol. 88, 1–26. https://doi.org/10.2113/gsecongeo.88.1.1.

Farrokhpay, S., Cathelineau, M., Blancher, S.B., Laugier, O., Filippov, L., 2019. Characterization of Weda Bay nickel laterite ore from Indonesia. J. Geochem. Explor. 196, 270–281. https://doi.org/10.1016/j.gexplo.2018.11.002.

Freyssinet, P., Butt, C.R.M., Morris, R.C., Piantone, P., 2005. Ore-forming processes related to lateritic weathering. Econ. Geol. 681-722 doi:10.5382/AV100.21.

Gao, D., Sheng, Z., Shi, S., Chen, L., 1992. Studies on the Bauxite Deposit in Central Guizhou, China. Guizhou Science & Technology Publishing House, Guiyang (In Chinese).

Goldhaber, M.B., 2003. Sulfur-rich sediments. In: D HH, K TK (Eds.), Treatise on Geochemistry Vol 7 Sediments, Diagenesis and Sedimentary Rocks, pp. 257–288.

Griffin, W.L.,Powell, W.J.,Pearson, N.J., O'Reilly, S.Y., 2008. GLITTER: Data reduction software for laser ablation ICP-MS, In: Sylvester, P. (Eds.), Laser Ablation-ICP-MS in the Earth Sciences: Current Practices and Outstanding Issues. Mineralogical Association Canada Short Course, vol. 40, pp. 308–311.

Gu, J., Huang, Z.L., Fan, H.P., Jin, Z.G., Yan, Z.F., Zhang, J.W., 2013. Mineralogy, geochemistry, and genesis of lateritic bauxite deposits in the Wuchuan–Zheng'an–Daozhen area, Northern Guizhou Province, China. J. Geochem. Explor. 130, 44–59.

Guilcher, M., Schmaucks, A., Krause, J., Markl, G., Gutzmer, J., Burisch, M., 2021. Vertical zoning in hydrothermal U-Ag-Bi-Co-Ni-As systems: a case study from the Annaberg-Buchholz district, Erzgebirge (Germany). Econ. Geol. 116, 1893–1915. https://doi.org/10.5382/econgeo.4867.

Guizhou Bureau of Geology and Mineral Resources, 1987. Geological Features of Guizhou Province. Geological Publishing House, Beijing (in Chinese).

Habicht, K.S., Canfield, D.E., Rethmeier, J.O., 1998. Sulfur isotope fractionation during bacterial reduction and disproportionation of thiosulfate and sulfite. Geochim. Cosmochim. Acta 62, 2585–2595. https://doi.org/10.1016/S0016-7037(98)00167-7.

Habicht, K.S., Gade, M., Thamdrup, B., Berg, P., Canfield, D.E., 2002. Calibration of sulfate levels in the Archean Ocean. Science 298, 2372–2374. https://doi.org/10.1126/science.1078265.

Hou, Y.L., Zhong, Y.T., Xu, Y.G., He, B., 2017. The provenance of late Permian karstic bauxite deposits in SW China, constrained by the geochemistry of interbedded clastic rocks, and U–Pb–Hf–O isotopes of detrital zircons. Lithos 278, 240–254. https://doi.org/10.1016/j.lithos.2017.01.013.

Hou, Z.Q., Chen, J., Zhai, M.G., 2020. Current status and frontiers of research on critical mineral resources. Chin. Sci. Bull. 65, 3651–3652 (in Chinese with English abstract).

Huang, Z.L., Jin, Z.G., Xiang, X.L., Gu, J., Wu, G.H., Chen, X.L., Su, Z.L., Zhao, Y.Y., Ye, L., Zhou, L., 2014. Deposit Geochemistry. In: Wang, Y. (Ed.), Metallogenic Theory and Prediction of Bauxite Deposits in the Wuchuan-Zhengan-Daozhen Area, Northern Guizhou Province, China. Science Press, Beijing, pp. 89–99 (in Chinese).

Hughes, H.S., Mcdonald, I., Faithfull, J.W., Upton, B.G., Loocke, M., 2016. Cobalt and precious metals in sulphides of peridotite xenoliths and inferences concerning their distribution according to geodynamic environment: a case study from the Scottish lithospheric mantle. Lithos 240, 202–227. https://doi.org/10.1016/j.lithos.2015.11.007.

Jefferson, C.W., Thomas, D.J., Gandhi, S.S., Ramaekers, P., Delaney, G., Brisbin, D., Cutts, C., Portella, P., Olson, R.A., 2007. Unconformity-associated uranium deposits of the Athabasca Basin, Saskatchewan and Alberta. Bull. Geol. Surv. Can. 588, 23–67.

Jiang, S.Y., Yang, J.H., Ling, H.F., Chen, Y.Q., Feng, H.Z., Zhao, K.D., Ni, P., 2007. Extreme enrichment of polymetallic Ni–Mo–PGE–Au in lower Cambrian black shales of South China: an Os isotope and PGE geochemical investigation. Palaeogeogr. Palaeoclimatol. Palaeoecol. 254, 217–228. https://doi.org/10.1016/j.palaeo.2007.03.024.

Kamenetsky, V.S., Lygin, A.V., Foster, J.G., Meffre, S., Maas, R., Kamenetsky, M.B., Goemann, K., Beresford, S.W., 2016. A story of olivine from the McIvor Hill complex (Tasmania, Australia): Clues to the origin of the Avebury metasomatic Ni sulfide deposit. Am. Mineral. 101, 1321–1331. https://doi.org/10.2138/am-2016-5509.

Kampschulte, A., Strauss, H., 2004. The sulfur isotopic evolution of Phanerozoic seawater based on the analysis of structurally substituted sulfate in carbonates. Chem. Geol. 204, 255–286. https://doi.org/10.1016/j.chemgeo.2003.11.013.

Khosravi, M., Abedini, A., Alipour, S., Mongelli, G., 2017. The Darzi-Vali bauxite deposit, West-Azarbaidjan Province, Iran: critical metals distribution and parental affinities. J. Afr. Earth Sci. 129, 960–972. https://doi.org/10.1016/j.jafrearsci.2017.02.024.

Khosravi, M., Vérard, C., Abedini, A., 2021. Palaeogeographic and geodynamic control on the Iranian karst-type bauxite deposits. Ore Geol. Rev. 139, 104589 https://doi.org/10.1016/j.oregeorev.2021.104589.
Laskou, M., Economou-Eliopoulos, M., 2007. The role of microorganisms on the mineralogical and geochemical characteristics of the Parnassos-Ghiona bauxite deposits, Greece. J. Geochem. Explor. 93, 67–77. https://doi.org/10.1016/j.gexplo.2006.08.014.
Ling, K.Y., Zhu, X.Q., Wang, Z.G., Han, T., Tang, H.S., Chen, W.Y., 2013. Metallogenic model of bauxite in Central Guizhou Province: an example of Lindai deposit. Acta Geol. Sin. 87, 1630–1642. https://doi.org/10.1111/1755-6724.12164.
Ling, K.Y., Zhu, X.Q., Tang, H.S., Wang, Z.G., Yan, H.W., Han, T., Chen, W.Y., 2015. Mineralogical characteristics of the karstic bauxite deposits in the Xiuwen ore belt, Central Guizhou Province, Southwest China. Ore Geol. Rev. 65, 84–96. https://doi.org/10.1016/j.oregeorev.2014.09.003.
Ling, K.Y., Zhu, X.Q., Tang, H.S., Li, S.X., 2017. Importance of hydrogeological conditions during formation of the karstic bauxite deposits, Central Guizhou Province, Southwest China: a case study at Lindai deposit. Ore Geol. Rev. 82, 198–216. https://doi.org/10.1016/j.oregeorev.2016.11.033.
Ling, K.Y., Zhu, X.Q., Tang, H.S., Du, S.J., Gu, J., 2018. Geology and geochemistry of the Xiaoshanba bauxite deposit, Central Guizhou Province, SW China: Implications for the behavior of trace and rare earth elements. J. Geochem. Explor. 190, 170–186. https://doi.org/10.1016/j.gexplo.2018.03.007.
Ling, K.Y., Tang, H.S., Zhang, Z.W., Wen, H.J., 2020. Host minerals of Li–Ga–V–rare earth elements in Carboniferous karstic bauxites in Southwest China. Ore Geol. Rev. 119, 325–337. https://doi.org/10.1016/j.oregeorev.2020.103325.
Liu, H., Beaudoin, G., 2021. Geochemical signatures in native gold derived from Au-bearing ore deposits. Ore Geol. Rev. 132, 104066 https://doi.org/10.1016/j.oregeorev.2021.104066.
Liu, W.H., Borg, S.J., Testemale, D., Etschmann, B., Hazemann, J.-L., Brugger, J., 2011. Speciation and thermodynamic properties for cobalt chloride complexes in hydrothermal fluids at 35–440°C and 600bar: an in-situ XAS study. Geochim. Cosmochim. Acta 75, 1227–1248. https://doi.org/10.1016/j.gca.2010.12.002.
Liu, X.F., Wang, Q.F., Deng, J., Zhang, Q.Z., Sun, S.L., Meng, J.Y., 2010. Mineralogical and geochemical investigations of the Dajia Salento-type bauxite deposits, western Guangxi, China. J. Geochem. Explor. 105, 137–152. https://doi.org/10.1016/j.gexplo.2010.04.012.
Liu, X.F., Wang, Q.F., Feng, Y.W., Li, Z.M., Cai, S.H., 2013. Genesis of the Guangou karstic bauxite deposit in western Henan, China. Ore Geol. Rev. 55, 162–175. https://doi.org/10.1016/j.oregeorev.2013.06.002.
Liu, X.F., Wang, Q.F., Zhang, Q.Z., Yang, S.J., Liang, Y.Y., Zhang, Y., Li, Y., Guan, T., 2017. Genesis of the Permian karstic Pingguo bauxite deposit, western Guangxi, China. Mineral. Deposita 52, 1031–1048. https://doi.org/10.1007/s00126-017-0723-y.
Long, Y.Z., Chi, G.X., Liu, J.P., Jin, Z.G., Dai, T.G., 2017. Trace and rare earth elements constraints on the sources of the Yunfeng paleo-karstic bauxite deposit in the Xiuwen-Qingzhen area, Guizhou, China. Ore Geol. Rev. 91, 404–418. https://doi.org/10.1016/j.oregeorev.2018.07.013.
Long, Y.Z., Lu, A.H., Gu, X.P., Chi, G.X., Ye, L., Jin, Z.G., Zhang, D.L., 2020. Cobalt enrichment in a paleo-karstic bauxite deposit at Yunfeng, Guizhou Province, SW China. Ore Geol. Rev. 117, 308–320. https://doi.org/10.1016/j.oregeorev.2019.103308.
Loukola-Ruskeeniemi, K., 1999. Origin of black shales and the serpentinite-associated Cu-Zn-Co ores at Outokumpu, Finland. Econ. Geol. 94, 1007–1028. https://doi.org/10.2113/gsecongeo.94.7.1007.
Loukola-Ruskeeniemi, K., Lahtinen, H., 2013. Multiphase evolution in the black-shale-hosted Ni–Cu–Zn–Co deposit at Talvivaara, Finland. Ore Geol. Rev. 52, 85–99. https://doi.org/10.1016/j.oregeorev.2012.10.006.
Machel, H.G., 2001. Bacterial and thermochemical sulfate reduction in diagenetic settings—old and new insights. Sediment. Geol. 140, 143–175. https://doi.org/10.1016/S0037-0738(00)00176-7.
Maksimovic, Z., Pantó, G., 2004. Rare earth elements and nickel in the Grebnik diasporic bauxite deposit, Metohija (Kosovo). Acta Geol. Hung. 47, 259–268. https://doi.org/10.1556/ageol.47.2004.2-3.9.
Mameli, P., Mongelli, G., Oggiano, G., Dinelli, E., 2007. Geological, geochemical and mineralogical features of some bauxite deposits from Nurra (Western Sardinia, Italy): insights on conditions of formation and parental affinity. Int. J. Earth Sci. 96, 887–902. https://doi.org/10.1007/s00531-006-0142-2.
Mao, J.W., Lehmann, B., Du, A.D., Zhang, G.D., Ma, D.S., Wang, Y.T., Zeng, M.G., Kerrich, R., 2002. Re-Os dating of polymetallic Ni-Mo-PGE-Au mineralization in lower Cambrian black shales of South China and its geologic significance. Econ. Geol. 97, 1051–1061. https://doi.org/10.2113/gsecongeo.97.5.1051.
Markl, G., Burisch, M., Neumann, U., 2016. Natural fracking and the genesis of five-element veins. Mineral. Deposita 51, 703–712. https://doi.org/10.1007/s00126-016-0662-z.
Migdisov, A.A., Zezin, D., Williams-Jones, A.E., 2011. An experimental study of Cobalt (II) complexation in Cl^- and H_2S-bearing hydrothermal solutions. Geochim. Cosmochim. Acta 75, 4065–4079. https://doi.org/10.1016/j.gca.2011.05.003.
Mondillo, N., Balassone, G., Boni, M., Rollinson, G., 2011. Karst bauxites in the Campania Apennines (southern Italy): a new approach. Period. Mineral. 80, 407–432. https://doi.org/10.2451/2011PM0028.
Mongelli, G., Boni, M., Buccione, R., Sinisi, R., 2014. Geochemistry of the Apulian karst bauxites (southern Italy): chemical fractionation and parental affinities. Ore Geol. Rev. 63, 9–21. https://doi.org/10.1016/j.oregeorev.2014.04.012.
Mongelli, G., Buccione, R., Gueguen, E., Langone, A., Sinisi, R., 2016. Geochemistry of the apulian allochthonous karst bauxite, Southern Italy: distribution of critical elements and constraints on late cretaceous Peri-Tethyan palaeogeography. Ore Geol. Rev. 77, 246–259. https://doi.org/10.1016/j.oregeorev.2016.03.002.
Mongelli, G., Boni, M., Oggiano, G., Mameli, P., Sinisi, R., Buccione, R., Mondillo, N., 2017. Critical metals distribution in Tethyan karst bauxite: the cretaceous Italian ores. Ore Geol. Rev. 86, 526–536. https://doi.org/10.1016/j.oregeorev.2017.03.017.
Ohmoto, H., Goldhaber, M.B., 1997. Sulfur and carbon isotopes. In: Barnes, H.L. (Ed.), Geochemistry of Hydrothermal Ore Deposits. John Wiley, New York, pp. 517–611.
Öztürk, H.S., Hein, J.R., Hanilçi, N., 2002. Genesis of the Dogankuzu and Mortas Bauxite deposits, Taurides, Turkey: separation of Al, Fe, and Mn and implications for passive margin metallogeny. Econ. Geol. 97, 1063–1077. https://doi.org/10.2113/gsecongeo.97.5.1063.
Qiu, Z.J., Fan, H.R., Goldfarb, R., Tomkins, A.G., Yang, K.F., Li, X.C., Xie, L.W., Liu, X., 2021. Cobalt concentration in a sulfidic sea and mobilization during orogenesis: Implications for targeting epigenetic sediment-hosted Cu-Co deposits. Geochim. Cosmochim. Acta 305, 1–18. https://doi.org/10.1016/j.gca.2021.05.001.
Radusinović, S., Jelenković, R., Pačevski, A., Simić, V., Božović, D., Holclajtner-Antunović, I., Životić, D., 2017. Content and mode of occurrences of rare earth elements in the Zagrad karstic bauxite deposit (Nikšić area, Montenegro). Ore Geol. Rev. 80, 406–428. https://doi.org/10.1016/j.oregeorev.2016.05.026.
Roberts, S., Gunn, G., 2014. Cobalt. In: Gunn, G. (Ed.), Critical Metals Handbook. John Wiley & Sons, American Geophysical Union, British Geological Survey, Keyworth, pp. 134–135.
Rong, J.Y., Chen, X., Wang, Y., Zhan, R.B., Liu, J.B., Huang, B., Tang, P., Wu, R.C., Wang, G.X., 2011. Northward expansion of Central Guizhou Oldland through the Ordovician and Silurian transition: evidence and implications. Sci. Sin. Terrae 41, 1407–1415 (in Chinese with English abstract).
Salamab Ellahi, S., Taghipour, B., Zarasvandi, A., Bird, M.I., Somarin, A.K., 2016. Mineralogy, geochemistry and stable isotope studies of the Dopolan bauxite deposit, Zagros Mountain, Iran. Minerals 6, 11. https://doi.org/10.3390/min6010011.
Scharrer, M., Kreissl, S., Markl, G., 2019. The mineralogical variability of hydrothermal native element-arsenide (five-element) associations and the role of physicochemical and kinetic factors concerning sulfur and arsenic. Ore Geol. Rev. 113, 025–052. https://doi.org/10.1016/j.oregeorev.2019.103025.
Scharrer, M., Epp, T., Walter, B., Pfaff, K., Vennemann, T., Markl, G., 2021. The formation of (Ni-Co-Sb)-Ag-As ore shoots in hydrothermal galena-sphalerite-fluorite veins. Mineral. Deposita 57, 853–885. https://doi.org/10.1007/s00126-021-01059-y.
Sinisi, R., 2018. Mineralogical and geochemical features of Cretaceous bauxite from San Giovanni Rotondo (Apulia, Southern Italy): a provenance tool. Minerals. 8, 567. https://doi.org/10.3390/min8120567.
Slack, J.F., 2012. Strata-bound Fe-Co-Cu-Au-Bi-Y-REE deposits of the Idaho cobalt belt: Multistage hydrothermal mineralization in a magmatic-related iron oxide copper-gold system. Econ. Geol. 107, 1089–1113. https://doi.org/10.2113/econgeo.107.6.1089.
Temur, S., Kansun, G., 2006. Geology and petrography of the Masatdagi diasporic bauxites, Alanya, Antalya, Turkey. J. Asian Earth Sci. 27, 512–522. https://doi.org/10.1016/j.jseaes.2005.07.001.
Tian, Y., Etschmann, B., Liu, W.H., Borg, S., Mei, Y., Testemale, D., O'neill, B., Rae, N., Sherman, D.M., Ngothai, Y., Johannessen, B., Glover, C., Brugger, J., 2012. Speciation of nickel (II) chloride complexes in hydrothermal fluids: in situ XAS study. Chem. Geol. 334, 345–363. https://doi.org/10.1016/j.chemgeo.2012.10.010.
Ugwu, I.M., Sherman, D.M., 2017. Irreversibility of sorption of cobalt to goethite (α-FeOOH) and disparities in dissolution of aged synthetic Co-goethite. Chem. Geol. 467, 168–176. https://doi.org/10.1016/j.chemgeo.2017.08.011.
Vasyukova, O., Williams-Jones, A., 2022. Constraints on the genesis of cobalt deposits: Part II. Applications to natural systems. Econ. Geol. 117, 529–544. https://doi.org/10.5382/econgeo.4888.
Veloso, A.S.R., Monteiro, L.V.S., Juliani, C., 2020. The link between hydrothermal nickel mineralization and an iron oxide-copper–gold (IOCG) system: constraints based on mineral chemistry in the Jatobá deposit, Carajás Province. Ore Geol. Rev. 121, 103555 https://doi.org/10.1016/j.oregeorev.2020.103555.
Wang, R.X., 2019. Mineral Compositions and Metallogenic Mechanism of Important Bauxite Concentration Areas in China (Dissertation). China University of Geoscience, Beijing (in Chinese with English abstract).
Wang, R.X., Wang, Q.F., Huang, Y.X., Yang, S.J., Liu, X.F., Zhou, Q., 2018. Combined tectonic and paleogeographic controls on the genesis of bauxite in the early Carboniferous to Permian Central Yangtze Island. Ore Geol. Rev. 101, 468–480. https://doi.org/10.1016/j.oregeorev.2018.07.013.
Wang, Y.F., Wang, Z.L., Lu, A.H., Wu, L., Xu, D.R., Wu, T., Long, Y.Z., Huang, Z.L., Fan, H.P., Peng, E.K., 2021. Discovery of cobalt-rich pyrite in the Yangjiadong ore block of the Maochang bauxite deposit, Guizhou Province and its significance. Acta Mineral. Sin. 41, 460–474 (in Chinese with English abstract).
Wang, Z.Z., Yang, W.T., Fan, X.G., Liu, W.B., Yan, K., Wang, L.W., 2019. Geochemical characteristics and metallogenic regularity of bauxite deposits in Guanmiao-Daping area, Henan. Miner. Explor. 10, 1082–1092 (in chinese with English abstract).
Wen, J., Zhang, Y.X., Wen, H.J., Ling, K.Y., Zhu, C.W., Fan, H.F., Shen, N.P., 2021. Gallium isotope fractionation in the Xiaoshanba bauxite deposit, Central Guizhou Province, southwestern China. Ore Geol. Rev. 137, 104299 https://doi.org/10.1016/j.oregeorev.2021.104299.
Whitney, D.L., Evans, B.W., 2010. Abbreviations for names of rock-forming minerals. Am. Mineral. 95, 185–187. https://doi.org/10.2138/am.2010.3371.
Williams-Jones, A., Vasyukova, O., 2022. Constraints on the genesis of cobalt deposits: part I. Theoretical considerations. Econ. Geol. 117, 513–528. https://doi.org/10.5382/econgeo.4895.

Wu, L., Huang, Z.L., Wang, Z.L., Wang, Y.F., Chen, J., Wu, T., 2021. Geochemistry of bauxite in the Maochang deposit, Central Guizhou. Acta Mineral. Sin. 41, 475–484 (in Chinese with English abstract).

Xiong, G.L., Yu, W.C., Du, Y.S., Weng, S.F., Pang, D.W., Deng, X.S., Zhou, J.T., 2021. Provenance of lower carboniferous bauxite deposits in Northern Guizhou, China: Constraints from geochemistry and detrital zircon U-Pb ages. J. Earth Sci. 32, 235–252. https://doi.org/10.1007/s12583-020-1081-8.

Xu, E.Z., 2018. Studying on distribution and characteristics of chemical elements of Shenjiagou bauxite in Dengfeng City, Henan. Miner. Explor. 9, 62–69 (in Chinese with English abstract).

Xue, C.J., Chi, G.X., Fayek, M., 2015. Micro-textures and in situ sulfur isotopic analysis of spheroidal and zonal sulfides in the giant Jinding Zn–Pb deposit, Yunnan, China: implications for biogenic processes. J. Asian Earth Sci. 103, 288–304. https://doi.org/10.1016/j.jseaes.2014.07.009.

Yang, S.J., Huang, Y.X., Wang, Q.F., Deng, J., Liu, X.F., Wang, J.Q., 2019. Mineralogical and geochemical features of karst bauxites from Poci (western Henan, China), implications for parental affinity and bauxitization. Ore Geol. Rev. 105, 295–309. https://doi.org/10.1016/j.oregeorev.2018.12.028.

Yang, S.J., Wang, Q.F., Lai, X.L., Qiao, L., Wang, R.X., Huang, Y.X., Wang, Y.Z., 2021. Genesis of end-Guadalupian bauxite and pyrite deposits in the Youjiang Basin (South China): Insights into the causative link between magmatic events and mass extinction. J. Asian Earth Sci. 215, 104801 https://doi.org/10.1016/j.jseaes.2021.104801.

Yao, J.L., Shu, L.S., Santosh, M., Zhao, G.C., 2014. Neoproterozoic arc-related mafic–ultramafic rocks and syn-collision granite from the western segment of the Jiangnan Orogen, South China: constraints on the Neoproterozoic assembly of the Yangtze and Cathaysia Blocks. Precambrian Res. 243, 39–62. https://doi.org/10.1016/j.precamres.2013.12.027.

Yu, W.C., Wang, R.H., Zhang, Q.L., Du, Y.S., Chen, Y., Liang, Y.P., 2014. Mineralogical and geochemical evolution of the Fusui bauxite deposit in Guangxi, South China: from the original Permian orebody to a Quarternary Salento-type deposit. J. Geochem. Explor. 146, 75–88. https://doi.org/10.1016/j.gexplo.2014.07.020.

Yu, W.C., Algeo, T.J., Du, Y.S., Zhang, Q.L., Liang, Y.P., 2016. Mixed volcanogenic–lithogenic sources for Permian bauxite deposits in southwestern Youjiang Basin, South China, and their metallogenic significance. Sediment. Geol. 341, 276–288. https://doi.org/10.1016/j.sedgeo.2016.04.016.

Yu, W.C., Algeo, T.J., Yan, J.X., Yang, J.H., Du, Y.S., Huang, X., Weng, S.F., 2019. Climatic and hydrologic controls on upper Paleozoic bauxite deposits in South China. Earth Sci. Rev. 189, 159–176. https://doi.org/10.1016/j.earscirev.2018.06.014.

Zamanian, H., Ahmadnejad, F., Zarasvandi, A., 2016. Mineralogical and geochemical investigations of the Mombi bauxite deposit, Zagros Mountains, Iran. Geochem. 76, 13–37. https://doi.org/10.1016/j.chemer.2015.10.001.

Zarasvandi, A., Carranza, E.J.M., Ellahi, S.S., 2012. Geological, geochemical, and mineralogical characteristics of the Mandan and Deh-now bauxite deposits, Zagros Fold Belt, Iran. Ore Geol. Rev. 48, 125–138. https://doi.org/10.1016/j.oregeorev.2012.02.010.

Zeng, W.J., 2019. The geology characteristics of high-sulfur bauxite in the Maochang bauxite deposit, Guizhou. Res. Inf. Eng. 34, 29–30 (in Chinese with English abstract).

Zhao, G.C., 2015. Jiangnan Orogen in South China: developing from divergent double subduction. Gondwana Res. 27, 1173–1180. https://doi.org/10.1016/j.gr.2014.09.004.

Zhou, Y.F., Wang, R.C., Lu, J.J., Li, Y.L., 2006. Ferruginous Microspherules in Bauxite at Maochang, Guizhou Province, China: Products of Microbe-Pyrite Interaction? Acta Geol. Sin. 80, 604–609. https://doi.org/10.1111/j.1755-6724.2006.tb00281.x.

Zhuang, Z.X., Tao, Y.C., Zhou, A.L., 2016. Genesis discussion of Maochang Super-large Bauxite deposit. Guizhou. Geol. 33, 272–283 (in Chinese with English abstract).